

Polythiophenes comprising conjugated pendants toward long-term air-stable inverted polymer solar cells with high open circuit voltages

Cite this: *J. Mater. Chem. A*, 2013, **1**, 8950

Hsing-Ju Wang,^a Chen-Wei Chou,^b Chih-Ping Chen,^{*c} Ying-Hsiao Chen,^b Rong-Ho Lee^{*b} and Ru-Jong Jeng^{*a}

A series of polythiophenes (PTs) functionalized with bulky conjugated side chains comprising *tert*-butyl substituted carbazole (tCz) as an electron donor pendant and bisbenzothiazolylvinyl (DBT) as an electron acceptor pendant were synthesized via Stille copolymerization for polymer solar cell (PSC) applications. We use the descriptors PTtCz, PT(tCz)_{0.9}(DBT)_{0.1}, PT(tCz)_{0.64}(DBT)_{0.36}, PT(tCz)_{0.45}(DBT)_{0.55}, and PTDBT to identify each of these conjugated polymers, with the names denoting the compositions of the bulky pendants. The tunable energy levels of the PTs were accomplished by incorporating both tCz as a donor pendant and DBT as an acceptor pendant, while retaining the low-lying HOMO levels (−5.26 to −5.39 eV). Furthermore, lower bandgaps were observed for the DBT-derived PTs because of stronger donor– π –acceptor characteristics and more efficient intramolecular charge transfer. Conventional PSCs were fabricated by spin-coating the blend of each PT and the fullerene derivative (PC₇₁BM). The conventional PSC devices exhibited high open circuit voltages (V_{oc}) of around 0.79–0.91 V. The power conversion efficiency (PCE) of the PSCs based on PTtCz : PC₇₁BM (w/w = 1 : 2.5) reached 2.48% with a V_{oc} of 0.91 V, short circuit current (J_{sc}) of 6.58 (mA cm^{−2}) and fill factor (FF) of 41% under the illumination of AM1.5, 100 mW cm^{−2}. Furthermore, a PTtCz/PC₇₁BM-based inverted PSC with ZnO_x and MoO₃ as an electron extraction layer and a hole extraction layer respectively was capable of retaining ca. 80% of its original efficiency after storage under ambient conditions (without encapsulation) for 1032 h, according to the ISOS-D-1 shelf protocol. The highly durable inverted PSC accompanied by a large V_{oc} value was achieved for the PT-type polymers.

Received 29th March 2013

Accepted 16th May 2013

DOI: 10.1039/c3ta11272a

www.rsc.org/MaterialsA

Introduction

Wet-processing is the main advantage of polymer solar cells (PSC). In this process, the active layer can be manufactured using fast roll-to-roll based methods at a cost that has the potential to be competitive, pending further development.^{1–5} On the basis of the concept of the bulk heterojunction (BHJ) structure, PSCs made by blending poly(3-hexylthiophene) (P3HT) as a donor and fullerene derivative [6,6]-phenyl-C₆₁/71-butyric acid methyl ester (PC₆₁BM/PC₇₁BM) as an acceptor have been intensively investigated, leading to power conversion efficiencies (PCE) of up to 4–5%.^{6–8} Unfortunately, the highest occupied molecular orbital (HOMO) (−4.9 to −5.1 eV) energy level of P3HT resulted in an unsatisfactory open circuit voltage

(V_{oc}) value of only about 0.6 V and narrow absorption spectra in the UV-visible region which limited the photocurrent generation of its related BHJ solar cell.⁹ In general, the V_{oc} of a PSC is proportional to the difference between the HOMO of the electron-sufficient polymer and the lowest unoccupied molecular orbital (LUMO) of the electron-deficient fullerene. Lower HOMO levels of the polymers would provide a higher V_{oc} according to the theoretical prediction. Additionally, conjugated polymers with higher ionization potentials are capable of minimizing the p-doping level under ambient O₂ and increasing the environmental stability.¹⁰

Much of the improvement in PSCs can be attributed to the design of novel conjugated polymers with (i) strong and broad visible absorption with high charge carrier mobility to increase the short-circuit current density (J_{sc}) and (ii) low-lying HOMO levels to achieve large V_{oc} values. The absorption properties and the energy levels can be modulated by introducing conjugated side chains onto the conjugated polymers.^{11,12} Li and coworkers first studied a PT with conjugated pendants attached that exhibited a broad absorption band in the UV and visible regions, and was capable of harvesting a great amount of solar light.¹³ Subsequently, the investigations on PTs comprising

^aInstitute of Polymer Science and Engineering, National Taiwan University, Taipei 106, Taiwan. E-mail: rujong@ntu.edu.tw; Fax: +886-2-33665237; Tel: +886-2-33665884

^bDepartment of Chemical Engineering, National Chung Hsing University, Taichung 402, Taiwan. E-mail: rhl@nchu.edu.tw; Fax: +886-4-22854734; Tel: +886-4-22854308

^cDepartment of Materials Engineering, Ming Chi University of Technology, New Taipei City 243, Taiwan. E-mail: cpchen@mail.mcut.edu.tw; Fax: +886-2-29084091; Tel: +886-2-29089899 extn. 4439

conjugated pendants as side-chains have attracted a great deal of interest.^{14–19} Our previous studies on conjugated polymers presenting bulky conjugated electron donor moieties as side-chains revealed that the sterically induced twisting of the polymer backbone was responsible for achieving a low-lying HOMO level and enhancing the oxidative stability of conjugated polymers as compared to the parent P3HT.^{20,21} Larger V_{oc} values of the conjugated PTs functionalized with bulky pendants have been observed in conventional PSCs.^{13,22–24} Nevertheless, the bulky substituents increase the degree of twisting from planarity in the backbone, resulting in a decreased intramolecular charge transfer and larger optical bandgaps (E_g). To address this issue, the incorporation of electron acceptor pendants on PTs was studied by Wei and coworkers.^{17,18} The results showed that a lower E_g was obtained due to the presence of the efficient intramolecular charge transfer from the PT backbone to the conjugated acceptor side chain induced by the electron-accepting imidazole moiety.

To systematically investigate the variation of photophysical properties and energy levels *via* the strategy of developing PTs with covalently attached both electron donor and acceptor pendants, we first synthesized PTs functionalized with various contents of *tert*-butyl substituted carbazole (*tCz*) as an electron donor pendant^{25,26} and bisbenzothiazolylvinyl (DBT) as an electron acceptor pendant.^{27,28} The synthesis, properties and PSC performances of the novel PTs comprising 2-ethylhexyl-substituted quaterthiophene (T) as the conjugated unit in the PT backbone along with different composition ratios of *tCz* and DBT as bipolar pendant groups were reported in this study (Scheme 1). According to the literature,²⁹ the optical and electronic properties of the polymers can be easily manipulated through the attachment of electron-withdrawing groups while taking the variation of the acceptor strengths into account. Therefore, one would anticipate further energy level adjustment when the acceptor moiety DBT is incorporated. Depending on the copolymer composition of PTs comprising conjugated pendants, samples such as PT*tCz*, PT(*tCz*)_{0.9}(DBT)_{0.1}, PT(*tCz*)_{0.64}(DBT)_{0.36}, PT(*tCz*)_{0.45}(DBT)_{0.55}, and PTDBT were synthesized and investigated (Scheme 1). To validate the dual-adjustment of the lower-lying HOMO levels and narrow E_g values, UV-vis absorption spectroscopy and cyclic voltammetry (CV) were employed to study the effect of bipolar pendants on the photophysical and electrochemical properties of the PT-based copolymers. We fabricated conventional PSCs by spin-coating the solutions of PT-based

copolymers/PC₇₁BM blends, and then the dried films were sandwiched between a transparent anode ITO and cathodes (Ca/Al). The PV performance of these PSCs was studied in terms of the influence of the conjugated pendant groups. Additionally, in order to investigate the important issue of air stability, the PT*tCz* based inverted devices without encapsulation were tested under ambient conditions for 1032 h, under the ISOS-D-1 shelf measurement.^{30,31}

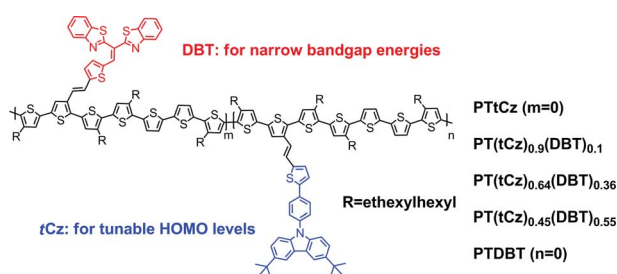
Experimental

Chemicals

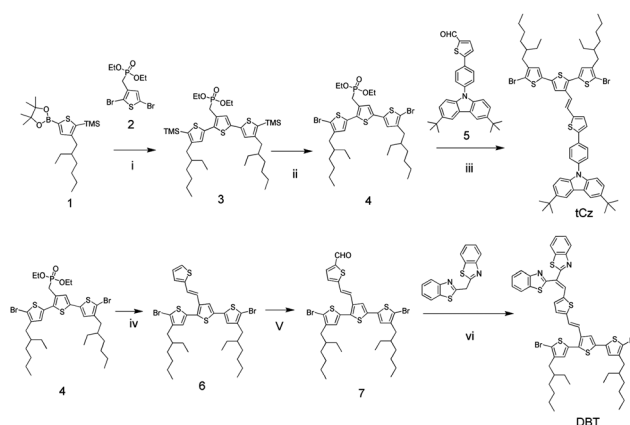
Trimethylstannyl chloride, *n*-bromosuccinimide, 2-formylthiophene, phosphorous oxychloride, 2,2'-methylene bisbenzothiazole, *n*-butyllithium (2.5 M in hexane) and other reagents and chemicals were purchased from Aldrich, Alfa and TCI Chemical Co., and used as received. Dichloromethane (DCM), tetrahydrofuran (THF), dimethylformamide (DMF), toluene, and *o*-dichlorobenzene (*o*-DCB) were freshly distilled over appropriate drying agents prior to use, while being purged with nitrogen. The *tert*-butyl-substituted carbazole-containing moiety (*tCz*) and 2, 2'-methylenebisbenzothiazole substituted moiety (DBT) were synthesized according to Scheme 2. Syntheses of a series of PTs-based donor-acceptor random copolymers *via* Stille polymerization with various *tCz*/DBT feed ratios are illustrated in Scheme 3. Compounds 2-(4-ethylhexyl-5-trimethylsilylthiophen-2-yl)-4,4,5,5-tetramethyl-1,3,2]dioxaborolane (1), diethyl(2,5-dibromothiophen-3-yl)methylphosphonate (2), 5-(4-(3,6-di-*tert*-9-carbazolyl)phenyl)thiophene-2-carbaldehyde (5) and 5,5'''-dibromo-3,3'''-diethylhexyl-2,2'; 5',2''; 5'',2'''-quater-thiophene were synthesized according to the literature.^{22,32}

Synthesis of compound (3)

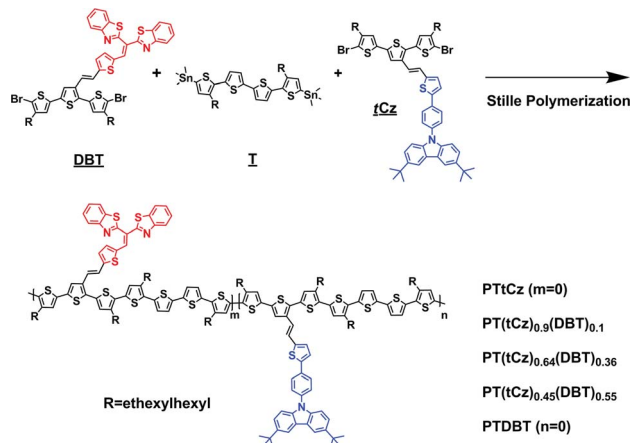
A mixture of compound (2) (0.58 g, 1.5 mmol), compound (1) (1.21 g, 3.3 mmol), and Pd(PPh₃)₄ (0.037 g, 0.03 mmol) was dissolved in a degassed mixture of toluene (12 mL) and 2 M



Scheme 1 PTs comprising bipolar pendant groups.



Scheme 2 Synthesis of the conjugated pendants *tCz* and DBT (i) Pd(PPh₃)₄, 2M K₂CO₃ (aq.), toluene, reflux, 8 h; (ii) NBS, AcOH, DCM, 0 °C, 1 h; (iii) CH₃ONa, DMF, 0 °C, 2 h; (iv) 2-carboxaldehyde, potassium *tert*-butoxide, THF, 0 °C, 1 h; (v) DMF, phosphoryl chloride, dichloroethane, from 0 °C to reflux, 8 h; (vi) 2,2'-methylenebisbenzothiazole, I₂, K₂CO₃, DMF, 60 °C, 6 h.



Scheme 3 Reaction scheme for preparing the PT-based random copolymers.

$\text{K}_2\text{CO}_3(\text{aq})$ (12 mL). The solution was stirred at reflux temperature for 48 h, and then poured into methanol (100 mL). The crude product was partitioned between EA and water, and the organic phase was dried (MgSO_4), filtered, and evaporated to dryness. The residue was purified using silica gel chromatography (EA : hexane = 1 : 10) to give a yellow liquid (0.72 g, yield = 63%). $^1\text{H-NMR}$ (δ/ppm , CDCl_3): 0.28 (s, 18H), 0.84 (m, 18H), 1.22 (m, 16H), 1.55 (m, 2H), 2.58 (m, 4H), 3.25 (d, $J = 6.4$ Hz, 2H), 4.02 (m, 4H), 7.05 (s, 1H), 7.15 (m, 2H).

Synthesis of compound (4)

Compound (3) (6.22 g, 10 mmol) was dissolved in DCM (25 mL). The solution was then stirred in an ice water bath for 15 minutes. *N*-bromosuccinimide (3.55 g, 20 mmol) was dissolved in a mixture of DCM (20 mL) and AcOH (10 mL). This mixture was then added dropwise to the compound (3) solution over 15 min at 0 °C. The reaction mixture was warmed to room temperature and stirred for 2 h. Subsequently, Na_2SO_3 aqueous solution was added to quench the reaction. The mixture was partitioned between EA–water, and the organic phase was dried (MgSO_4), filtered, and evaporated to dryness. The residue was purified using silica gel chromatography (EA : hexane = 1 : 10) to give a yellow liquid (5.72 g, yield = 81%). $^1\text{H-NMR}$ (δ/ppm , 400 MHz, CDCl_3): 0.86 (m, 18H), 1.23 (m, 16H), 1.58 (m, 2H), 2.42 (m, 4H), 3.18 (d, $J = 5.2$ Hz, 2H), 4.02 (m, 4H), 6.80 (s, 1H), 6.84 (s, 1H), 7.08 (s, 1H).

Synthesis of compound tCz

A mixture of compound (4) (7.81 g, 10 mmol) and CH_3ONa (1.78 g, 33 mmol) in 30 mL DMF was stirred under an ice water bath for several minutes. Compound (5) (4.66 g, 10 mmol) was then added to the solution. After 2 h, the reaction was quenched with methanol and a yellow powder was precipitated. Further purification was performed using silica gel chromatography (hexane as eluent) to give a yellow solid (7.19 g, yield = 66%). $^1\text{H-NMR}$ (δ/ppm , 400 MHz, CDCl_3): 0.82 (m, 12H), 1.29 (m, 16H), 1.44 (s, 18H), 1.59 (m, 2H), 2.48 (m, 4H), 6.85 (d, $J = 1.2$ Hz, 2H), 7.07 (m, 3H), 7.25 (d, $J = 8.8$ Hz, 1H), 7.28 (d, $J = 7.6$ Hz, 1H),

7.38 (d, $J = 0.8$ Hz, 2H), 7.44 (m, 2H), 7.54 (d, $J = 9.2$ Hz, 2H), 7.77 (d, $J = 4$ Hz, 2H), 8.12 (t, $J = 1.6$ Hz, 2H). ESIMS (m/z): calcd for $\text{C}_{60}\text{H}_{69}\text{Br}_2\text{NS}_4$: 1092.26. Found: 1092.4. Anal calcd for $\text{C}_{50}\text{H}_{50}\text{Br}_2\text{N}_2\text{S}_6$: C, 65.98; H, 6.37; N, 1.28. Found: C, 65.72; H, 6.44; N, 1.14%.

Synthesis of compound (6)

A mixture of compound (4) (7.81 g, 10 mmol) and K_2CO_3 (2.76 g, 20 mmol) in 30 mL dry THF was stirred under an ice water bath for 15 minutes. A solution of 2-carbadehydethiophene (1.68 g, 15 mmol) in dry THF (7 mL) was then added to the mixture. After 2 h, the reaction was quenched with methanol. Further purification was performed using silica gel chromatography (hexane as eluent) to give a yellow oil (4.95 g, yield = 67%). $^1\text{H-NMR}$ (δ/ppm , 400 MHz, CDCl_3): 0.87 (m, 12H), 1.27 (m, 16H), 1.52 (m, 2H), 2.45 (m, 4H), 6.81 (d, $J = 10$ Hz, 1H), 6.98 (m, $J = 8.4$ Hz, 1H), 7.02 (s, 1H), 7.05 (s, 1H), 7.08 (d, $J = 3.2$ Hz, 1H), 7.14 (s, 1H), 7.19 (d, $J = 5.2$ Hz, 1H), 7.23 (d, $J = 3.6$ Hz, 1H).

Synthesis of compound (7)

POCl_3 (7.45 mL, 80 mmol) was added dropwise to freshly distilled DMF (3.09 mL, 40 mmol) at 0 °C under nitrogen atmosphere. Compound 6 (7.39 g, 10 mmol) dissolved in dichloroethane (50 mL) was added dropwise to the above-mentioned POCl_3/DMF complex at room temperature. The reaction mixture was stirred at 80 °C for 3 h. Subsequently, the reaction was cooled to 0 °C and 2 M NaOH aqueous solution was added to quench the reaction. The mixture was partitioned between EA–water, and the organic phase was dried (MgSO_4), filtered, and evaporated to dryness. The residue was purified using silica gel chromatography (EA : hexane = 1 : 10) to give a yellow oil (5.09 g, 77%). $^1\text{H-NMR}$ (δ/ppm , 400 MHz, CDCl_3): 0.86 (m, 12H), 1.27 (m, 16H), 1.59 (m, 2H), 2.45 (m, 4H), 6.81 (d, $J = 10.4$ Hz, 1H), 7.06 (s, 1H), 7.10 (s, 1H), 7.12 (d, $J = 2.8$ Hz, 1H), 7.23 (d, $J = 2.4$ Hz, 1H), 7.25 (d, $J = 4.0$ Hz, 1H), 7.63 (d, $J = 5.6$ Hz, 1H), 9.89 (s, 1H).

Synthesis of compound DBT

A mixture of dibenzo[d]thiazol-2-ylmethane (3.11 g, 11 mmol), K_2CO_3 (0.04 g, 0.3 mmol), and I_2 (0.07 g, 0.3 mmol) in 20 mL DMF was stirred under room temperature for 15 minutes. A solution of compound 7 (7.67 g, 10 mmol) in DMF (15 mL) was added to the mixture, and then the reaction solution was heated to 60 °C. After 2 h, the reaction was quenched with methanol. The mixture was partitioned between EA–water, and the organic phase was dried (MgSO_4), filtered, and evaporated to dryness. Further purification was performed using silica gel chromatography (EA : hexane = 1 : 10) to give a red solid (7.43 g, yield = 72%). $^1\text{H-NMR}$ (δ/ppm , CDCl_3): 0.86 (m, 12H), 1.28 (m, 16H), 1.54 (m, 2H), 2.43 (m, 4H), 6.76 (d, $J = 8.0$ Hz, 2H), 6.87 (s, 1H), 6.91 (d, $J = 13.6$ Hz, 1H), 6.98 (d, $J = 6.4$ Hz, 2H), 7.15 (s, 1H), 7.19 (t, $J = 4.4$ Hz, 1H), 7.31 (t, $J = 16.4$ Hz, 1H), 7.49 (t, $J = 12.8$ Hz, 2H), 7.55 (t, $J = 16.8$ Hz, 1H), 7.79 (d, $J = 7.6$ Hz, 1H), 7.99 (d, $J = 8$ Hz, 2H), 8.16 (s, 1H), 8.22 (d, $J = 8.4$ Hz, 1H). ESIMS (m/z): calcd for $\text{C}_{50}\text{H}_{50}\text{Br}_2\text{N}_2\text{S}_6$: 1031.14 Found: 1031.0. Anal

calcd for $C_{50}H_{50}Br_2N_2S_6$: C, 58.24; H, 4.89; N, 2.72; S, 18.66
Found: C, 58.24; H, 4.86; N, 2.77; S, 18.52%.

Synthesis of compound T

A solution of 5,5'''-dibromo-3,3'''-diethylhexyl-2,2'; 5',2''; 5'',2'''-quaterthiophene (7.12 g, 10 mmol) in dry THF (150 mL) was stirred at -78°C under a N_2 atmosphere and then *n*-BuLi (2.5 M in hexane, 8.40 mL, 21 mmol) was added dropwise to the solution. The solution mixture was maintained at -78°C with stirring for 1 h, at which point trimethyltinchloride (4.98 g, 25 mmol) in dry THF (5 mL) was added dropwise. The mixture was warmed to room temperature and stirred for 8 h. Subsequently, HCl (1 N) was added to quench the reaction. The resulting mixture was partitioned between EA and water, and the organic phase was dried ($MgSO_4$), filtered, and evaporated to dryness. The residue was purified using silica gel chromatography (hexane, with 1% TEA) to give a greenish oil (7.13 g, yield = 81%). $^1\text{H-NMR}$ (δ /ppm, 400 MHz, $CDCl_3$): 0.82 (m, 12H), 1.07 (m, 18H), 1.23 (m, 16H), 1.52 (m, 2H), 2.71 (m, 4H), 6.89 (s, 2H), 6.98 (d, $J = 3.6$ Hz, 2H), 7.08 (d, $J = 4$ Hz, 2H). ESIMS (m/z): calcd for $C_{38}H_{58}S_4Sn_2$: 880.55 Found: 880.2. Anal calcd for $C_{38}H_{58}S_4Sn_2$: C, 51.83; H, 6.64 Found: C, 52.10; H, 6.74%.

Synthesis of PTtCz

A solution of tCz (1.64 g, 1.5 mmol) and T (1.32 g, 1.5 mmol) in dry toluene (20 mL) was purged with N_2 and subjected to three freeze-pump-thaw cycles to remove traces of O_2 . $Pd(PPh_3)_4$ (30 mg, 1 mol%) was added to the mixture, which was then stirred and heated under reflux for 48 h. After cooling to room temperature, the mixture was poured into MeOH (100 mL) and the precipitated material was filtered through a Soxhlet thimble. Soxhlet extractions were performed sequentially with MeOH, hexane, acetone, and $CHCl_3$. The polymer was recovered through rotary evaporation of the $CHCl_3$ fraction. Drying the sample under vacuum for 24 h provided an orange-red solid (70%). Gel permeation chromatography (GPC; THF): weight-average molecular weight (M_w), 21 421 $g\ mol^{-1}$; polydispersity index (PDI), 2.35. $^1\text{H-NMR}$ (δ /ppm, 400 MHz, $CDCl_3$): 1.01 (br, 42H), 1.30–1.34 (br, 32H), 1.57–1.62 (br, 4H), 2.30–2.46 (br, 8H), 6.40–7.50 (br, 15H), 7.55 (br, 2H), 7.79 (br, 2H), 8.12 (br, 4H).

Synthesis of PT(tCz)_{0.9}(DBT)_{0.1}

Using the same procedure as that described for the synthesis of PTtCz, the reaction of tCz (1.24 g, 1.13 mmol), DBT (0.38 g, 0.37 mmol), and T (1.32 g, 1.5 mmol) gave a dark-red solid (67%). GPC: M_w , 41 531 $g\ mol^{-1}$; PDI, 3.49. $^1\text{H-NMR}$ (δ /ppm, 400 MHz, $CDCl_3$): 1.01 (br, 84H), 1.30–1.34 (br, 64H), 1.57–1.62 (br, 8H), 2.60–2.80 (br, 16H), 6.40–7.50 (br, 33H), 7.55 (br, 2H), 7.79 (br, 3H), 7.88 (br, 1H), 7.99 (br, 1H), 8.16 (br, 4H), 8.22 (br, 1H).

Synthesis of PT(tCz)_{0.64}(DBT)_{0.36}

Using the same procedure as that described for the synthesis of PTtCz, the reaction of tCz (0.82 g, 0.75 mmol), DBT (0.77 g, 0.75 mmol), and T (1.32 g, 1.5 mmol) gave a dark-red solid (64%). GPC: M_w , 34 235 $g\ mol^{-1}$; PDI, 3.23. $^1\text{H-NMR}$ (δ /ppm, 400 MHz,

$CDCl_3$): 0.87 (br, 84H), 1.26–1.30 (br, 64H), 1.45–1.56 (br, 8H), 2.62–2.84 (br, 16H), 6.94–7.46 (br, 33H), 7.56 (br, 2H), 7.80 (br, 3H), 7.89 (br, 1H), 8.01 (br, 1H), 8.14 (br, 4H), 8.19 (br, 1H).

Synthesis of PT(tCz)_{0.45}(DBT)_{0.55}

Using the same procedure as that described for the synthesis of PTtCz, the reaction of tCz (0.40 g, 0.37 mmol), DBT (1.16 g, 1.13 mmol), and T (1.32 g, 1.5 mmol) gave a dark-red solid (60%). GPC: M_w , 28 875 $g\ mol^{-1}$; PDI, 2.93. $^1\text{H-NMR}$ (δ /ppm, 400 MHz, $CDCl_3$): 0.88 (br, 84H), 1.27–1.30 (br, 64H), 1.46–1.70 (br, 8H), 2.72 (br, 16H), 6.95–7.46 (br, 33H), 7.57 (br, 2H), 7.80 (br, 3H), 7.91 (br, 1H), 8.01 (br, 1H), 8.14 (br, 4H), 8.20 (br, 1H).

Synthesis of PTDBT

Using the same procedure as that described for the synthesis of PTtCz, the reaction of DBT (1.54 g, 1.5 mmol) and T (1.32 g, 1.5 mmol) gave a dark-red solid (65%). GPC: M_w , 29 616 $g\ mol^{-1}$; PDI, 3.49. $^1\text{H-NMR}$ (δ /ppm, 400 MHz, $CDCl_3$): 0.89 (br, 84H), 1.30–1.34 (br, 64H), 1.57–1.62 (br, 8H), 2.47–2.80 (br, 16H), 6.90–7.31 (br, 18H), 7.77 (br, 1H), 7.88 (br, 1H), 7.98 (br, 1H), 8.17 (br, 1H).

Characterization of copolymers

$^1\text{H-NMR}$ (400 MHz) spectra were recorded using a Varian Unity Inova spectrometer. The average molecular weights of the polymers were measured by means of GPC on a Waters chromatography system (717 plus Autosampler) equipped with two Waters Styragel linear columns. Polystyrene standards were used, with THF as the eluent. The glass transition temperature (T_g) and thermal decomposition temperature (T_d , the temperature at which weight loss reaches 5%) of the copolymers were determined by means of differential scanning calorimetry (TA Instruments, DSC-2010) and thermogravimetric analysis (TA Instruments, TGA-2050), respectively. Both analyses were performed under N_2 atmosphere at a scanning (both heating and cooling) rate of $10^\circ\text{C}\ \text{min}^{-1}$. The absorption spectra were measured using a Hitachi U3010 UV-Vis spectrometer. Fluorescence spectra were measured using a Varian Cary Eclipse luminescence spectrometer. Dilute *o*-DCB solutions of the PTs were filtered through a 0.45 μm filter to remove insoluble materials before spectral measurements. Redox potentials of the polymers were determined with a CHI 611D electrochemical analyser (scanning rate: $50\ \text{mV}\ \text{s}^{-1}$) equipped with Pt electrodes and an Ag/Ag^+ (0.10 M $AgNO_3$ in MeCN) reference electrode in an anhydrous, N_2 -saturated solution of 0.1 M Bu_4NClO_4 in MeCN. Bu_4NClO_4 (98%, TCI) was recrystallized three times from ethyl acetate and then dried at 60°C under reduced pressure. A Pt plate coated with a thin polymer film was used as the working electrode, a Pt wire and an Ag/Ag^+ electrode were used as the counter and reference electrodes, respectively. CV curves were calibrated using ferrocene as the standard, whose HOMO is set at $-4.8\ \text{eV}$ with respect to zero vacuum level. The $E_{\text{onset}}^{\text{ox}}$ of ferrocene/ferrocene $^+$ is 0.36 V in $Bu_4NClO_4/MeCN$ solution (0.1 M). The HOMO energy levels were obtained from the equation: $\text{HOMO} = -e(E_{\text{onset}}^{\text{ox}} - E_{\text{onset,ferrocene}}^{\text{ox}} + 4.8)$ (eV). The

LUMO levels of the polymer were obtained from the equation:

$$\text{LUMO} = -e(E_{\text{onset}}^{\text{red}} - E_{\text{onset,ferrocene}}^{\text{red}} + 4.8) \text{ (eV)}.$$
³³

Fabrication and characterization of PSCs³⁴

All the conventional PSCs in this study were based on a structure like the indium tin oxide (ITO)-coated glass/hole-transporting material (HTM)/photoactive layer/Ca (30 nm)/Al (100 nm) structure, in which the photoactive layer consisted of an interpenetrating network of PTs/PC₇₁BM. The ITO substrates (obtained from Sanyo, Japan ($8 \Omega \square^{-1}$)) were first patterned by lithography, cleaned with detergent, and ultrasonicated in acetone and isopropyl alcohol, dried on a hot plate at 120 °C for 5 min, and finally treated with oxygen plasma for 5 min. PC₇₁BM was purchased from Nano-C and used as received. Poly(3,4-ethylene-dioxythiophene):poly(styrenesulfonate) (PEDOT:PSS, Baytron P-VP A14083) was filtered through a 0.45 μm filter before being deposited on ITO, with a thickness around 30 nm, by spin coating at 3000 rpm in the air and drying at 150 °C for 30 min inside a glove box. A solution mixture of PTs-based donor-acceptor random copolymers and PC₇₁BM (10 mg mL⁻¹ in *o*-DCB) was stirred overnight, then filtered through a 0.2 μm poly(tetrafluoroethylene) (PTFE) filter and spin-coated (1200 rpm, 30 s) onto the PEDOT:PSS layer to prepare the PT/PC₇₁BM composite film-based photo-active layer. The optimal thickness of the active layers obtained under these conditions was *ca.* 60 nm. Subsequently, the device was completed by depositing *ca.* (30 nm) and Al (100 nm) under $<10^{-6}$ mm-Hg pressure, respectively. The active area of the conventional device was 5 mm². Finally the cell was encapsulated using UV-curing glue (obtained from Nagase, Japan). During the encapsulation process, the UV-glue was dispensed onto the edge of a piece of glass in the air. The UV-glue coated glass was transferred to the glove box for covering the PSC device. The device was then sealed by pressing the UV-glue coated glass on top of the device, and the device underwent UV curing (254 nm) for 2 min. Upon device encapsulation, the *I*-*V* curves of the PSC devices were measured in an ambient atmosphere at 25 °C using a computer-controlled Keithley 2400 source measurement unit (SMU) equipped with a Peccell solar simulator under AM 1.5G illumination (100 mW cm⁻²). The illumination intensity was calibrated using a standard Si photodiode detector equipped with a KG-5 filter. The output photocurrent was adjusted to match the photocurrent of the Si reference cell to obtain a power density of 100 mW cm⁻². An inverted device of PTtCz/PC₇₁BM-based film with the structure of ITO/ZnO_x/PTtCz:PC₇₁BM/MoO₃/Ag, in which ITO acted as the cathode and Ag as the anode, was prepared using the following procedure. A ZnO_x precursor solution was spin-cast on top of the pre-cleaned ITO-glass substrate. The films were annealed at 150 °C for 1 h in air. The ZnO_x film thickness was approximately 30 nm, as determined by a profilometer. The ZnO_x-coated substrates were then placed in a glove box. A photoactive layer, PTtCz:PC₇₁BM, was fabricated according to the condition for preparing the conventional device. Subsequently, a thin MoO₃ layer with a thickness of approximately 7 nm was vacuum-deposited on the top of the photoactive layer with an evaporation rate of 0.1 Å s⁻¹. In addition, the top electrode Ag

(50 nm) was thermally-deposited through a shade mask with an effective device area of 3 mm². The use of metal oxides on both sides of the PTtCz:PC₇₁BM layer would prevent the diffusion of moisture into the active layer. Under ambient atmosphere, the measurements of long-term photovoltaic characteristics of the PTtCz-derived inverted devices without encapsulation were performed in the same manner as those of the conventional devices as described above.

Results and discussion

Characterization of conjugated polymers

The molar ratios (*m/n*; Fig. 1) of the PTs were manipulated by controlling the feed ratios of the tCz/DBT conjugation units. In addition, the actual values of *m/n* were determined from the relative integral areas attributed to the peaks of tCz (7.48–7.50 ppm) and DBT (7.77–7.98 ppm and 8.17 ppm) by ¹H NMR spectra.^{22,28} The characteristic signals of tCz and DBT moieties are shown in Fig. 1 and indicated as blue and red arrows, respectively. The copolymer compositions were determined and named according to the actual ratios as indicated by PTtCz,

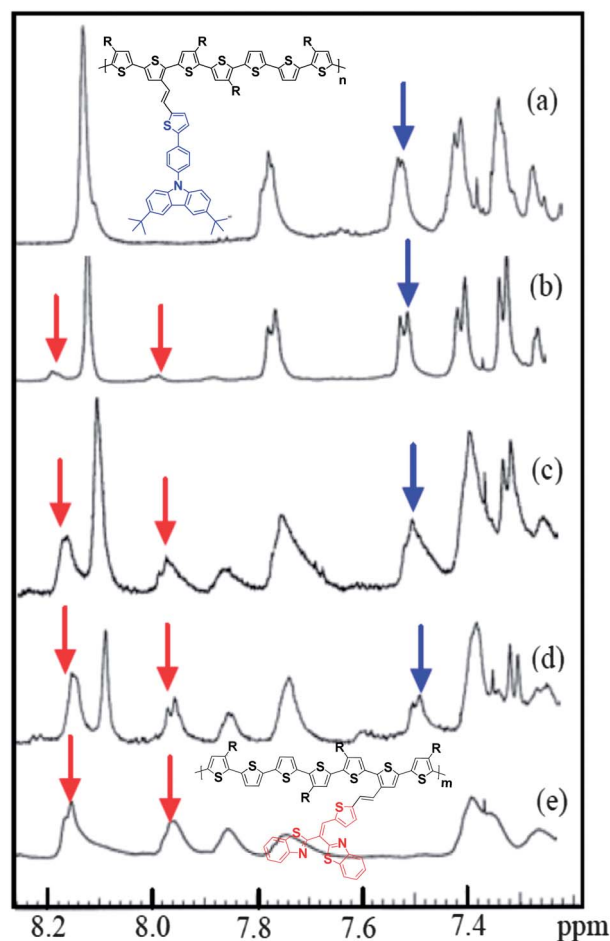


Fig. 1 ¹H NMR spectra of the PTs-based donor-acceptor random copolymers (a) PTtCz, (b) PT(tCz)_{0.9}(DBT)_{0.1}, (c) PT(tCz)_{0.64}(DBT)_{0.36}, (d) PT(tCz)_{0.45}(DBT)_{0.55}, and (e) PTDBT. The blue and red arrows indicate the characteristic signals of the tCz and DBT moieties, respectively.

PT(*t*Cz)_{0.9}(DBT)_{0.1}, PT(*t*Cz)_{0.64}(DBT)_{0.36}, PT(*t*Cz)_{0.45}(DBT)_{0.55}, and PTDBT. It is important to note that a higher actual *m/n* ratio was obtained despite the equal *t*Cz/DBT feed ratio during polymerization, for example in the case of PT(*t*Cz)_{0.64}(DBT)_{0.36}. This might be due to the fact that the relatively poor solubility of the DBT bulky segment would inhibit the propagation of the polymer chains. Furthermore, a higher content of DBT-containing segments would also lead to precipitation at the initial stages of polymerization, resulting in better propagation of the *t*Cz-containing segment. All of the conjugated copolymers were soluble in common organic solvents, including chloroform, THF, and *o*-DCB. In general, conjugated polymers exhibit poor solubility due to strong π - π interaction between planar polymer backbones. Moreover, the presence of the branched 2-ethylhexyl side-chains is effective in improving the solubility of conjugated copolymers. Using GPC with THF as the eluent and calibrating by a polystyrene standard, we determined the weight-average molecular weights (M_w s) and PDIs of the conjugated PTs. The values of M_w and PDI of PT*t*Cz, PT(*t*Cz)_{0.9}(DBT)_{0.1}, PT(*t*Cz)_{0.64}(DBT)_{0.36}, PT(*t*Cz)_{0.45}(DBT)_{0.55}, and PTDBT were (21 421, 2.35), (41 531, 3.49), (34 235, 3.23), (28 875, 2.93), and (29 616, 2.29), respectively.

The operational stability of the PSCs is directly related to the thermal stability of the conjugated polymers. Thus, high T_g s and T_d s are desirable for the conjugated polymers. T_d s (taken at 5 wt% weight loss) of PT*t*Cz, PT(*t*Cz)_{0.9}(DBT)_{0.1}, PT(*t*Cz)_{0.64}(DBT)_{0.36}, PT(*t*Cz)_{0.45}(DBT)_{0.55}, and PTDBT were 367, 348, 331, 355, and 288 °C, respectively. T_g s were determined from the second round of DSC heating scans. The T_g s of PT*t*Cz, PT(*t*Cz)_{0.9}(DBT)_{0.1}, PT(*t*Cz)_{0.64}(DBT)_{0.36}, PT(*t*Cz)_{0.45}(DBT)_{0.55}, and PTDBT were 122, 132, 120, 133, and 122 °C, respectively, which are considered to be good candidates for PSC applications in terms of thermal stability. A single endothermic glass transition was observed for each conjugated copolymer, implying that the electron-donating and electron-withdrawing bulky pendants (*t*Cz and DBT) were distributed homogeneously.

Optical properties of the conjugated polymers

The normalized UV-vis absorption spectra of the PTs in *o*-DCB solution and as solid films are shown in Fig. 2. Table 1 summarizes the photophysical properties of the copolymers. As shown in Fig. 2(a), the absorption bands of the PTs in *o*-DCB ranged from 325 to 600 nm, and each polymer exhibited a single broad absorption band. In general, PTs functionalized with conjugated pendants exhibit two maximum absorption peaks, one in the visible region attributed to the π - π^* transition of the conjugated polymer main chains, and the other in the UV region attributed to the conjugated side chains.^{16,35} In this study, the PTs functionalized with conjugated *t*Cz/DBT moieties showed only a single broad absorption peak. This indicates that a high degree of intramolecular conjugation was present within the conjugated frameworks of the polymers when in solution. Due to the electron withdrawing characteristic of the DBT moiety, the maximum absorption band located in the longer wavelength region would generally take place.^{27,28} Further red-shift of the maximum absorption wavelengths (Table 1) for the copolymer

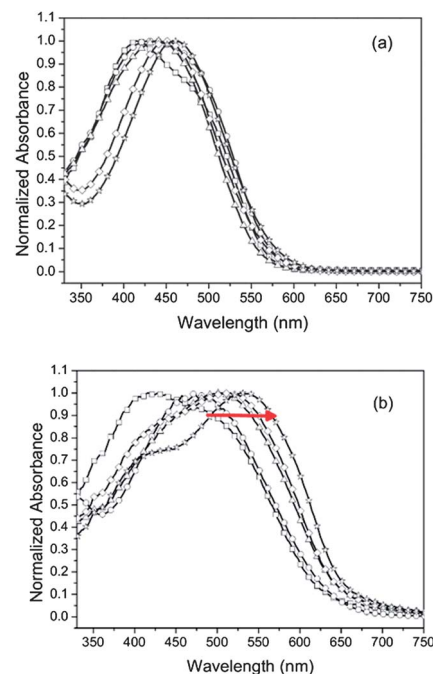


Fig. 2 UV spectra of PT-based random copolymers (a) in *o*-DCB and (b) as thin films. The symbols of the PTs are indicated as the following: PT*t*Cz (□), PT(*t*Cz)_{0.9}(DBT)_{0.1} (○), PT(*t*Cz)_{0.64}(DBT)_{0.36} (△), PT(*t*Cz)_{0.45}(DBT)_{0.55} (◇), and PTDBT (☆).

with increasing DBT content could be due to the stronger donor- π -acceptor characteristic and more efficient intramolecular charge transfer. As shown in Fig. 2(b), the absorption bands of the PTs as thin films were located between 350 and 650 nm. More red shift of the maximum absorption wavelengths and absorption edges was observed for these polymers as solid films than those in *o*-DCB. Bandgap energies (E_g s) of the conjugated PTs were determined from the onset wavelengths of their absorption bands. As shown in Table 1, the values of E_g were in the following order: PT*t*Cz (1.97) > PT(*t*Cz)_{0.9}(DBT)_{0.1} (1.96) > PT(*t*Cz)_{0.64}(DBT)_{0.36} (1.90) = PT(*t*Cz)_{0.45}(DBT)_{0.55} (1.90) > PTDBT (1.87) (eV). The E_g decreased with an increasing molar ratio of DBT in the PTs. In solution, these polymers exhibited absorption edges ranging from 550 to 580 nm which underwent a 50–70 nm red shift in the solid state. Interestingly, the PTDBT film revealed a broad and strong absorption band in the region from 350 to 650 nm, covering the UV and visible regions. This is because the incorporation of the electron-deficient DBT group results in a smaller E_g of the polymer. With increasing the DBT contents of the PTs, the stronger donor- π -acceptor characteristic and more efficient intramolecular charge transfer between the polymer backbones to conjugated pendants were manifested. Herein, the absorbance edge was extended from 570 to 650 nm for the PTs when the DBT content was increased to a certain extent. This indicates that using geometric donor- π -acceptor conjugated moieties as pendants in PTs is a feasible strategy to adjust the E_g of conjugated polymers. In other words, the photophysical properties can be tailored for the pursuit of better photovoltaic performance *via* the variation of the molar ratios of conjugated pendants.

Table 1 Optical properties and electronic energy levels of the PT-based random copolymers comprising donor and acceptor pendants

PTs	UV-visible absorption spectra				Cyclic voltammetry				
	$\lambda_{\max}^{\text{abs}}$ (nm) ^a	$\lambda_{\max}^{\text{abs}}$ (nm) ^b	$\lambda_{\text{onset}}^{\text{abs}}$ (nm) ^b	$E_{\text{g}}^{\text{opt}}$ (eV) ^c	$E_{\text{onset}}^{\text{ox}}$ (V)	HOMO (eV) ^d	$E_{\text{onset}}^{\text{red}}$ (V)	LUMO (eV) ^e	E_{g}^{ec} (eV) ^f
PTtCz	415	421	629	1.97	0.95	-5.39	-1.31	-3.13	2.26
PT(<i>t</i> Cz) _{0.9} (DBT) _{0.1}	433	475	634	1.96	0.87	-5.31	-1.30	-3.14	2.17
PT(<i>t</i> Cz) _{0.64} (DBT) _{0.36}	440	502	654	1.90	0.85	-5.29	-1.26	-3.18	2.11
PT(<i>t</i> Cz) _{0.45} (DBT) _{0.55}	450	517	655	1.90	0.84	-5.28	-1.23	-3.21	2.07
PTDBT	461	550	687	1.80	0.82	-5.26	-1.12	-3.32	1.94

^a The maximal absorption wavelength of the PTs in *o*-DCB. ^b The maximal absorption wavelength of the PTs as thin films. ^c Calculated from the onset absorption (λ_{onset}) of polymer thin films: $= 1240/\lambda_{\text{onset}}$. ^d The HOMO energy levels were obtained from the equation: $\text{HOMO} = -e(E_{\text{onset}}^{\text{ox}} - E_{\text{onset,ferrocene}}^{\text{ox}} + 4.8)$ (eV). ^e The LUMO levels of polymer were obtained from the equation: $\text{LUMO} = -e(E_{\text{onset}}^{\text{red}} - E_{\text{onset,ferrocene}}^{\text{red}} + 4.8)$ (eV). ^f Electrochemical bandgap energies $E = \text{LUMO} - \text{HOMO}$ (eV).

Electrochemical properties of the conjugated polymers

Since the PV performance of PSCs is closely related to the energy levels of the conjugated polymer, we determined the onset oxidation/reduction potentials of the PTs in air by employing cyclic voltammetry to calculate the HOMO/LUMO energy levels. This onset is defined by the intersection of the extrapolated baseline with the tangent to the inflection point. In Fig. 3, the onset oxidation potentials (E) of PTtCz, PT(*t*Cz)_{0.9}(DBT)_{0.1}, PT(*t*Cz)_{0.64}(DBT)_{0.36}, PT(*t*Cz)_{0.45}(DBT)_{0.55}, and PTDBT were 0.95, 0.87, 0.85, 0.84 and 0.82 V, respectively. The HOMO energy levels were calculated and listed in the order as following: PTtCz, (-5.39) < PT(*t*Cz)_{0.9}(DBT)_{0.1}, (-5.31) < PT(*t*Cz)_{0.64}(DBT)_{0.36}, (-5.29) < PT(*t*Cz)_{0.45}(DBT)_{0.55}, (-5.28) < PTDBT, (-5.26) (eV) (Table 1). These numbers are in an ideal range to ensure better air-stability and larger attainable V_{oc} in the device.³⁶ The onset reduction potentials (E) of PTtCz, PT(*t*Cz)_{0.9}(DBT)_{0.1}, PT(*t*Cz)_{0.64}(DBT)_{0.36}, PT(*t*Cz)_{0.45}(DBT)_{0.55}, and PTDBT were -1.31, -1.30, -1.26, -1.23, and -1.12 V, respectively. The LUMO energy levels were calculated and listed in the order as following: PTtCz, (-3.13) > PT(*t*Cz)_{0.9}(DBT)_{0.1}, (-3.14) > PT(*t*Cz)_{0.64}(DBT)_{0.36}, (-3.18) > PT(*t*Cz)_{0.45}(DBT)_{0.55},

(-3.21) > PTDBT, (-3.32) (eV). The electrochemical bandgap energies (E_{g}^{ec}) were calculated from the differences between the LUMO and HOMO energy levels (Table 1). The variations of electrochemical bandgap energies exhibited the same trend with those of the optical E_{g} s. The lower E_{g}^{ec} values for the PTs with an increasing content of DBT are attributed to the stronger donor- π -acceptor characteristic. The E_{g}^{ec} values of the studied PTs were 0.1–0.3 eV larger than the $E_{\text{g}}^{\text{opt}}$ values, which is probably due to the presence of the exciton binding energy of conjugated polymers.³⁷ The HOMO levels of PTs were shifted to low-lying values by ca. 0.48–0.35 eV when compared to that of P3HT. It is known that attachment of the *tert*-butyl groups on the electrochemically active sites of aromatic amines leads to better electrochemical stability.³⁸ Additionally, the dihedral angles formed between the 9-position substituted carbazole and benzene plane were approximately 60 ° along with two bulky *tert*-butyl group substituents, which inhibit the close π - π aggregation effectively between the polymer main chains.^{39,40} On the other hand, two vicinal benzothiazolyl substituents of donor-acceptor-substituted fluorine fluorophores are nearly perpendicular to each other from X-ray structure analysis.²⁸ The rigid benzothiazolyl substituents prevent the fluorine molecules from π - π interaction. In this study, the most critical factor in tailoring the oxidation potentials was the incorporation of bulky conjugated pendants capable of twisting adjacent thiophene rings through steric interactions, thereby reducing the π orbital overlapping of PTs backbones and resulting in the deeper HOMO energy levels. This phenomenon was more pronounced in the *t*Cz-derived polymers. Deeper HOMO energy levels were observed while the *t*Cz content was increased. In contrast, a weak acceptor DBT group does not significantly affect the oxidation potentials.²⁸ However, the attachment of the electron withdrawing group (DBT) onto the polymer backbone also had a positive effect in obtaining lower HOMO energy levels, as compared to the parent P3HT.⁹ PTs with an increasing content of DBT were still able to retain satisfactory anti-oxidation stability as compared to the oxygen energy level (-5.2 eV with respect to vacuum).^{10,41} As mentioned previously, the LUMO energy level is strongly influenced by the acceptor moiety.²⁸ Apparently, the LUMO energy levels decreased with an increasing DBT content of PTs in a significant manner. Indeed,

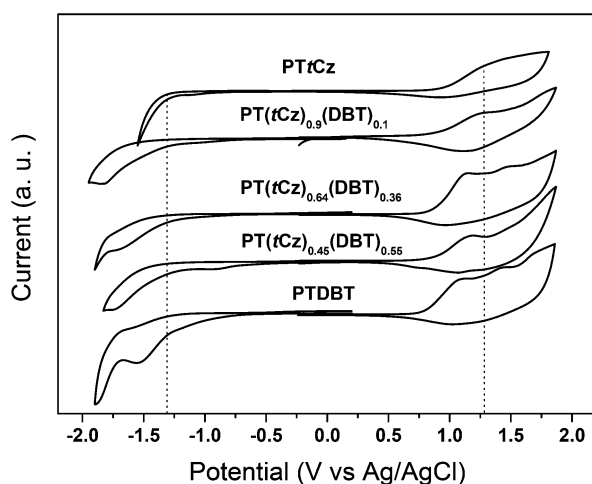


Fig. 3 Cyclic voltammograms of PT-based random copolymers thin films in a MeCN solution of 0.1 M TBAP at a scan rate of 50 mV S⁻¹.

the tunable energy levels of PTs were accomplished by incorporating both *t*Cz as donor pendants and DBT as acceptor pendants. This approach revealed a molecular design avenue to narrow the bandgap energies while retaining the low-lying HOMO levels.

PV properties of PSCs based on PT/PC₇₁BM films

PSCs were fabricated based on the ITO/PEDOT:PSS (30 nm)/PTs:PC₇₁BM/Ca (30 nm)/Al (100 nm) structure.³⁴ The optimum PTs/PC₇₁BM blend ratios were found to be 1 : 2.5 (w/w) and 1 : 3.5 (w/w) for PT*t*Cz-based and other PT-based photoactive films, respectively. Fig. 4 displays the *J*-*V* curves of each PTs/PC₇₁BM-based PSC, whereas the essential photovoltaic parameters (*V*_{oc}, *J*_{sc}, FF and PCE) are listed in Table 2. The devices based on PTs/PC₇₁BM all exhibited higher *V*_{oc} values (0.91–0.79 V), when compared with that of P3HT/PC₇₁BM (0.65 V).⁴² These high values of *V*_{oc} for the PT devices are consistent with their deeper HOMO energy levels. The *V*_{oc} value was decreased with increasing the DBT content in PTs, which is also consistent with the CV result. As expected, an excellent *V*_{oc} (0.91 V) value was observed for PT*t*Cz due to its deep HOMO energy level (−5.39 eV). Among these PT-based photoactive layers, the PT*t*Cz-based sample exhibited the best PCE (2.48%) because of its higher *J*_{sc} and largest *V*_{oc}, when compared with other samples in this study. One would have expected to further increase the PCE by introducing a DBT unit into the system. However, the PCE of PTDBT device was significantly limited by its low *J*_{sc} and *V*_{oc}, despite the fact that the UV-vis absorption spectrum of PTDBT was more red-shifted than that of PT*t*Cz. The results obtained in the PCE performances prompted us to further investigate the relevance of the charge transport properties of the PTs, which will be addressed in a later section. The lower photocurrent density might result from charge transport-related recombination losses. Additionally, the PCE of PT(*t*Cz)_{0.9}(DBT)_{0.1}/PC₇₁BM (0.89%) was the lowest among these PT-based PSCs. The presence of low molecular-weight fractions in the system (a rather broader PDI value (3.49) for PT(*t*Cz)_{0.9}(DBT)_{0.1}) would normally lead to a reduced

Table 2 Photovoltaic performances of the PTs/PC₇₁BM-based conventional PSCs

PTs	<i>V</i> _{oc} (V)	<i>J</i> _{sc} (mA cm ^{−2})	FF	PCE (%)
PT <i>t</i> Cz ^a	0.91	6.58	0.41	2.48
PT(<i>t</i> Cz) _{0.9} (DBT) _{0.1}	0.82	3.54	0.31	0.89
PT(<i>t</i> Cz) _{0.64} (DBT) _{0.36}	0.85	5.52	0.35	1.65
PT(<i>t</i> Cz) _{0.45} (DBT) _{0.55}	0.80	4.93	0.35	1.39
PDBT	0.79	5.05	0.33	1.31

^a PTs/PC₇₁BM = 1 : 2.5.

performance in photovoltaic parameters. It has been demonstrated that the broad molecular weight distributions of PTs are responsible for this dramatic decrease in performance, particularly those with low molecular weight fractions.⁴³ This phenomenon is caused by distinctly reduced charge carrier (hole) mobility in the donor phase of the devices built from the lower molecular-weight fractions of the PT samples.⁴⁴

Morphology of the thin films of PT/PC₇₁BM blends

The performance of a PSC is strongly dependent on the morphology of the conjugated polymer/fullerene derivative composite film. To generate more effective free carriers from bonding excitations and to avoid the recombination of excitons and free carriers, the P/N heterojunction phase must be controlled at the nanoscale level with an interpenetrating network. This is because the diffusion range of the exciton is approximately 10–20 nm.^{45,46} AFM was utilized to investigate the compatibility and morphology of the PT/PC₇₁BM composite films prepared in the same manner as those prepared in the device fabrication (Fig. 5, topographic (a) and phase (b) images). In each case, we observed a phase-separated interpenetrating network with sizable PC₇₁BM domains. The surface roughnesses of the PT/PC₇₁BM films were in the range of 0.21–0.32 nm. The overall small root mean square (RMS) values are probably due to the random conformation of the PTs and the presence of the steric bulky pendants in these PTs. These two factors prohibit the ordered packing of the polymer chains in the solid state.⁴⁷ The bulky pendants in the PTs provide sufficient free volume for the PC₇₁BM units to intercalate into the polymer chains. This could permit better compatibility between PC₇₁BM and the polymer chains. In Fig. 5(b), a certain degree of phase separation was observed, which is favorable for efficient formation of free carriers to provide optimal PV properties of PSCs. These results indicate that the compatibility and surface morphology of the PTs/PC₇₁BM films were influenced by the geometric structure of the pendants, but not by the presence of the electron donor or acceptor moieties.

Space charge limited current hole mobility

In addition to the morphology, we suspect that the variation of hole mobility might play an important role in influencing the device performance. To evaluate the contribution of polymer mobility, we employed hole-only devices using a high-work-function material, palladium (Pd), as the cathode to block the

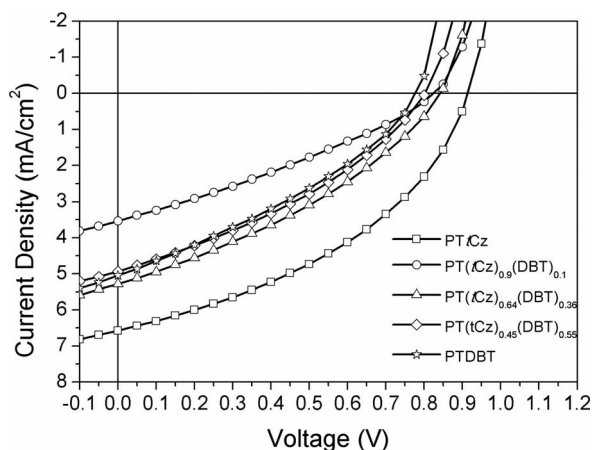


Fig. 4 Current density–potential curves of illuminated (AM 1.5 G, 100 mW cm^{−2}) PTs/PC₇₁BM-based conventional PSCs.

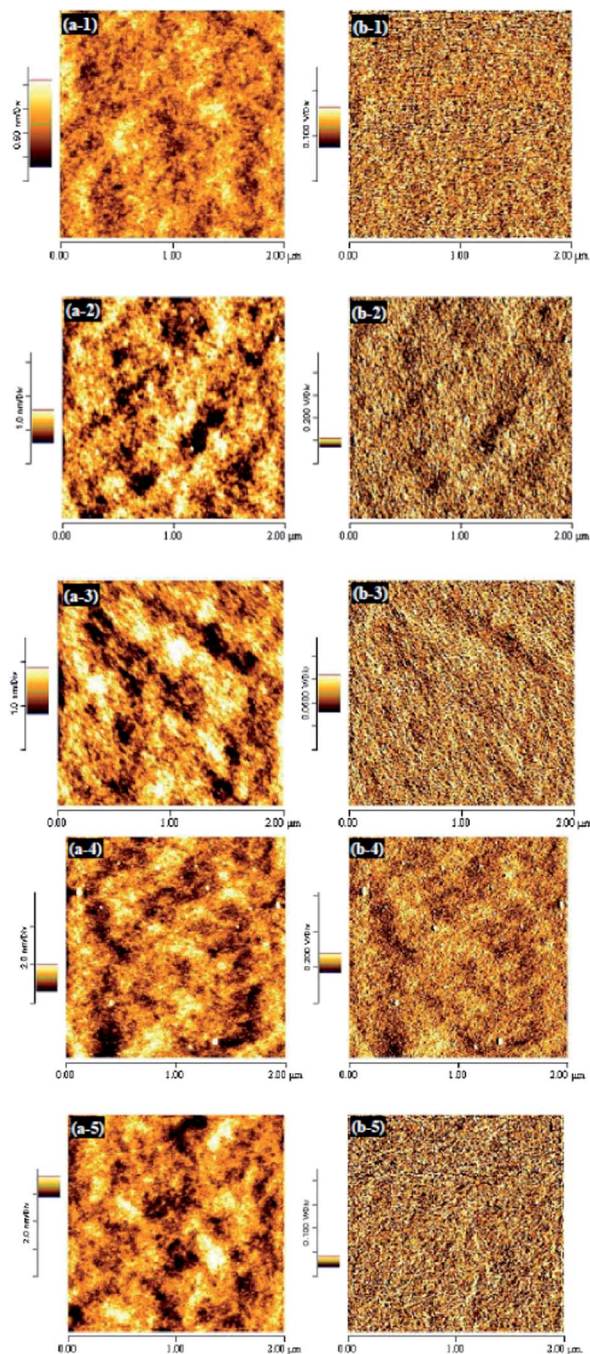


Fig. 5 AFM tapping mode topographic (a) and phase (b) images of fabricated photoactive PTs/PC₇₁BM-based blend thin films (1-PTtCz, 2-PT(tCz)_{0.9}(DBT)_{0.1}, 3-PT(tCz)_{0.64}(DBT)_{0.36}, 4-PT(tCz)_{0.45}(DBT)_{0.55}, and 5-PTDBT).

back injection of electrons.⁴⁸ When a sufficient voltage is applied to this hole-only device, the transport of holes through the polymer film is limited by the space charge that accumulates. The space charge limited current (SCLC) is described by eqn (1):

$$J = \frac{9}{8} \epsilon_r \epsilon_0 \mu_h \frac{V^2}{L^3} \quad (1)$$

Where ϵ_r is the dielectric constant of the polymer, ϵ_0 is the permittivity of free space, μ_h is the hole mobility, V is the voltage

applied to the device, and L is the blend film thickness. The experimental dark-current densities of the PTs devices were measured in the hole-only devices. The applied voltage was corrected for the built-in voltage (V_{BI}), which was estimated from the difference between the work function and the HOMO energy level of PTs. Based on the slopes from the plots of $J^{0.5}$ with respect to V for the corresponding devices, we calculated the field-independent mobilities of the PTtCz, PT(tCz)_{0.9}(DBT)_{0.1}, PT(tCz)_{0.64}(DBT)_{0.36}, and PT(tCz)_{0.45}(DBT)_{0.55} derived devices to be 1.35×10^{-5} , 9.19×10^{-6} , 9.23×10^{-6} , and 4.11×10^{-6} (cm² V⁻¹ s⁻¹), respectively. With increasing the tCz content in the PTs, higher hole mobility values were observed, which is consistent with the PCE performance mentioned earlier. This is attributed to the electron-donating character and more efficient π - π^* charge transfer of the carbazole moiety, which has been widely used as a hole transport material for organic electronics.²⁶ The increase in hole mobility exerts more influence on the J_{sc} value of the PTs-derived PSCs than the absorption characteristics. On the contrary, the losing hole mobility and lowering J_{sc} values were consistent for the PTs with increasing DBT content. The SCLC measurements are in good agreement with the PCE performances. With increasing the DBT content in the PTs, the presence of lower hole mobilities would lead to unbalanced charge transport and hole accumulation. The hole accumulation partially acted as the recombination centers of electron-hole pairs. Subsequently the photocurrent collection efficiency of the respective electrode was restricted.

Air stability of the PTtCz-derived inverted device

Our interests in understanding the air stability of our rationally designed low HOMO materials led us to evaluate their PCE degradation with time under ambient conditions. Due to the better environmental stability of the inverted cells,^{49–52} we further studied the durability of the PTtCz/PC₇₁BM-based film based on an inverted structure of ITO/ZnO_x/PTtCz:PC₇₁BM/MoO₃/Ag, as shown in Fig. 6(a). The long-term current density-potential characteristics of the PTtCz-derived inverted devices without encapsulation under ambient condition is shown in Table 3. The evaluated photovoltaic characteristics of the PTtCz/PC₇₁BM-based devices, as a function of elapsed time, are shown in Fig. 6(b). For each set of points in the plot, the average performance parameters of the devices were measured, and the standard deviation was recorded over an extended period of testing, further testifying the uniformity and robustness of the devices. As expected, the low-lying HOMO level of PTtCz (−5.39 eV), which is relatively stable against oxidation in ambient conditions allowed the device to retain *ca.* 80% of its original efficiency over a period of 1032 h (ISOS-D-1 shelf).^{30,31} Preliminary results indicate that this new synthetic material exhibited good stability in ambient conditions (defined as 25 °C/RH 50% in general) using an air-stable inverted architecture. Nevertheless, factors such as heat and humidity would affect the OPV performance in long-term practical applications.⁵³ Therefore, further long-term stability investigations are currently underway to understand the performance of inverted devices under outdoor conditions (ISOS-O-1 shelf).³¹

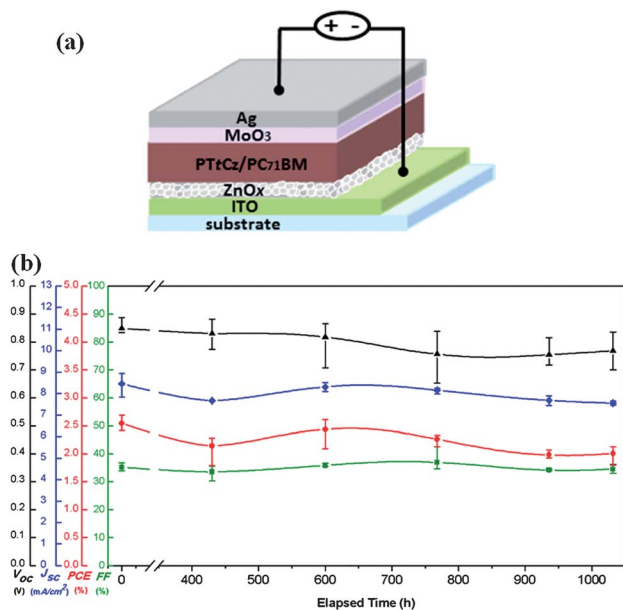


Fig. 6 (a) Architecture of the PTtCz/PC₇₁BM-based inverted PSC. (b) Summary plots for the long-term photovoltaic performances in ambient condition without encapsulation of the PTtCz/PC₇₁BM-based inverted PSC.

Table 3 Long-term photovoltaic performances of the PTtCz/PC₇₁BM-based inverted PSC in ambient conditions without encapsulation

Time (h)	V_{oc} (V)	J_{sc} (mA cm ⁻²)	FF	PCE (%)	Efficiency decay (%) ^a
0	0.86	8.43	0.36	2.58	—
430	0.85	7.67	0.35	2.26	12
600	0.85	8.30	0.36	2.55	1
768	0.76	8.13	0.38	2.30	11
936	0.76	7.68	0.34	1.98	23
1032	0.77	7.56	0.35	2.01	22

^a Based on its original conversion efficiency (0 h).

Conclusion

In conclusion, we synthesized a series of PT-based random copolymers functionalized with different composition ratios of tCz and DBT as bipolar pendant groups *via* Stille copolymerization. The dual-adjusted strategy towards narrow (1.97 to 1.80 eV) and lower-lying HOMO levels (−5.39 to −5.26 eV) of PTs were accomplished by incorporating both electron donor-tCz and acceptor-DBT pendants onto PTs. As expected, each PTs/PC₇₁BM PSC exhibited significantly high V_{oc} values (0.91 to 0.79 V) in the conventional device fabrication. The PSC based on PTtCz/PC₇₁BM (w/w = 1 : 2.5) reached a PCE of 2.48% under the illumination of AM 1.5, 100 mW cm⁻², along with a V_{oc} of 0.91 V, a J_{sc} of 6.58 mA cm⁻², and a FF of 41%. An inverted PSC without encapsulation based on PTtCz/PC₇₁BM as a photoactive layer, was capable of retaining *ca.* 80% of its original efficiency for 1032 h, according to the ISOS-D-1 shelf protocol. The excellent V_{oc} value for a long-term air stable inverted PSC based on a PT-type polymer using PCBM as an acceptor was achieved in this study.

Acknowledgements

We thank the National Science Council of Taiwan for financial support (grant numbers NSC-101-2221-E-002-035-MY3 and NSC101-2113-M-131-001-MY2).

Notes and references

- 1 D. Angmo, T. T. Larsen-Olsen, M. Jørgensen, R. R. Søndergaard and F. C. Krebs, *Adv. Energy Mater.*, 2013, **3**, 172.
- 2 N. Espinosa, M. Hosel, D. Angmo and F. C. Krebs, *Energy Environ. Sci.*, 2012, **5**, 5117.
- 3 X. Li, W. C. H. Choy, L. Huo, F. Xie, W. E. I. Sha, B. Ding, X. Guo, Y. Li, J. Hou, J. You and Y. Yang, *Adv. Mater.*, 2012, **24**, 3046.
- 4 L. Dou, J. You, J. Yang, C. C. Chen, Y. He, S. Murase, T. Moriarty, K. Emery, G. Li and Y. Yang, *Nat. Photonics*, 2012, **6**, 180.
- 5 Z. C. He, C. M. Zhong, S. J. Su, M. Xu, H. Wu and Y. Cao, *Nat. Photonics*, 2012, **6**, 591.
- 6 W. Ma, C. Yang, X. Gong, K. Lee and A. J. Heeger, *Adv. Funct. Mater.*, 2005, **15**, 1617.
- 7 Y. Kim, S. Cook, S. M. Tuladhar, S. A. Choulis, J. Nelson, J. R. Durrant, D. C. C. Bradley, M. Giles, I. McCulloch, C. S. Ha and M. Ree, *Nat. Mater.*, 2006, **5**, 197.
- 8 Y. J. Cheng, S. H. Yang and C. S. Hsu, *Chem. Rev.*, 2009, **109**, 5868.
- 9 G. Dennler, M. Scharber and C. J. Brabec, *Adv. Mater.*, 2009, **21**, 1323.
- 10 D. M. Leeuw, M. M. J. Simenon, A. R. Brown and R. E. F. Einerhand, *Synth. Met.*, 1997, **87**, 53.
- 11 Y. Li and Y. Zou, *Adv. Mater.*, 2008, **20**, 2952.
- 12 Y. Li, *Acc. Chem. Res.*, 2012, **45**, 723.
- 13 J. Hou, Z. A. Tan, Y. Yan, Y. He, C. Yang and Y. Li, *J. Am. Chem. Soc.*, 2006, **128**, 4911.
- 14 Z. G. Zhang, S. Zhang, J. Min, C. Chui, J. Zhang, M. Zhang and Y. Li, *Macromolecules*, 2011, **45**, 113.
- 15 J. H. Tsai, W. Y. Lee, W. C. Chen, C. Y. Yu, G. W. Hwang and C. Ting, *Chem. Mater.*, 2010, **22**, 3290.
- 16 C. Y. Yu, B. T. Ko, C. Ting and C. P. Chen, *Sol. Energy Mater. Sol. Cells*, 2009, **93**, 613.
- 17 Y. T. Chang, S. L. Hsu, M. H. Su and K. H. Wei, *Adv. Mater.*, 2009, **21**, 2093.
- 18 Y. T. Chang, S. L. Hsu, G. Y. Chen, M. H. Su, T. A. Singh, W. G. Diao and K. H. Wei, *Adv. Funct. Mater.*, 2008, **18**, 2356.
- 19 Z. G. Zhang, S. Y. Zhang, J. Min, C. H. Chui, J. Zhang, M. J. Zhang and Y. Li, *Macromolecules*, 2012, **45**, 113.
- 20 H. J. Wang, L. H. Chan, C. P. Chen, S. L. Lin, R. H. Lee and R. J. Jeng, *Polymer*, 2011, **52**, 326.
- 21 H. J. Wang, L. H. Chan, C. P. Chen, R. H. Lee, W. C. Su and R. J. Jeng, *Thin Solid Films*, 2011, **519**, 5264.
- 22 H. J. Wang, J. Y. Tzeng, C. W. Chou, C. Y. Huang, R. H. Lee and R. J. Jeng, *Polym. Chem.*, 2013, **3**, 506.
- 23 H. J. Wang, Y. P. Chen, Y. C. Chen, C. P. Chen, R. H. Lee, L. H. Chan and R. J. Jeng, *Polymer*, 2012, **53**, 4091.

- 24 S. Ko, E. T. Hoke, L. Pandey, S. Hong, R. Mondal, C. Risko, Y. Yi, R. Noriega, M. D. McGehee, J. L. Brédas, A. Salleo and Z. Bao, *J. Am. Chem. Soc.*, 2012, **134**, 5222.
- 25 O. Kwon, S. Barlow, S. A. Odom, L. Beverina, N. J. Thompson, E. Zojer, J. L. Brédas and S. R. Marder, *J. Phys. Chem. A*, 2005, **109**, 9346.
- 26 S. L. Lin, L. H. Chan, R. H. Lee, M. Y. Yen, W. J. Kuo, C. T. Chen and R. J. Jeng, *Adv. Mater.*, 2008, **20**, 3947.
- 27 C. L. Chiang, C. F. Shu and C. T. Chen, *Org. Lett.*, 2005, **7**, 3717.
- 28 C. L. Chiang, Y. J. Wen, Y. S. Wen, C. F. Shu and C. T. Chen, *J. Chin. Chem. Soc.*, 2006, **53**, 1325.
- 29 X. Zhang, T. T. Steckler, R. R. Dasari, S. Ohira, W. J. Potscavage Jr, S. P. Tiwari, S. Coppée, S. Ellinger, S. Barlow, J. L. Brédas, B. Kippelen, J. R. Reynolds and S. R. Marder, *J. Mater. Chem.*, 2010, **20**, 123.
- 30 M. O. Reese, S. A. Gevorgyan, M. Jørgensen, E. Bundgaard, S. R. Kurtz, D. S. Ginley, D. C. Olson, M. T. Lloyd, P. Morvillo, E. A. Katz, A. Elschner, O. Haillant, T. R. Currier, V. Shrotriya, M. Hermenau, M. Riede, K. R. Kirov, G. Trimmel, T. Rath, O. Inganäs, F. Zhang, M. Andersson, K. Tvingstedt, M. Lira-Cantu, D. Laird, C. McGuinness, S. Gowrisanker, M. Pannone, M. Xiao, J. Hauch, R. Steim, D. M. DeLongchamp, R. Rösch, H. Hoppe, N. Espinosa, A. Urbina, G. Yaman-Uzunoglu, J. Bonekamp, A. J. J. M. van Breemen, C. Girotto, E. Voroshazi and F. C. Krebs, *Sol. Energy Mater. Sol. Cells*, 2011, **95**, 1253.
- 31 M. Jørgensen, K. Norrman, S. A. Gevorgyan, T. Tromholt, B. Andreasen and F. C. Krebs, *Adv. Mater.*, 2012, **24**, 580.
- 32 A. C. Spivey, D. J. Turner, M. L. Turner and S. Yeates, *Org. Lett.*, 2002, **4**, 1899.
- 33 Y. J. Cheng, J. S. Wu, P. I. Shih, C. Y. Chang, P. C. Jwo, W. S. Kao and C. S. Hsu, *Chem. Mater.*, 2011, **23**, 2361.
- 34 C. P. Chen, Y. D. Chen and S. C. Chuang, *Adv. Mater.*, 2011, **23**, 3859.
- 35 Y. W. Li, H. J. Xia, B. Xu, S. P. Wen and W. J. Tian, *J. Polym. Sci., Part A: Polym. Chem.*, 2008, **46**, 3970.
- 36 M. C. Scharber, D. Mühlbacher, M. Koppe, P. Denk, C. Waldauf, A. J. Heeger and C. J. Brabec, *Adv. Mater.*, 2006, **18**, 789.
- 37 Y. Zhu, F. S. Kim, R. D. Champion and S. A. Jenekhe, *Macromolecules*, 2008, **411**, 7021.
- 38 H. M. Wang, S. H. Hsiao, G. S. Liou and C. H. Sun, *J. Polym. Sci., Part A: Polym. Chem.*, 2010, **48**, 4775.
- 39 Z. Ning, Q. Zhang, W. Wu, H. Pei, B. Liu and H. Tian, *J. Org. Chem.*, 2008, **73**, 3791.
- 40 D. J. Liaw, B. Y. Liaw, L. J. Li, B. Sillion, R. Mercier, R. Thiria and H. Sekiguchi, *Chem. Mater.*, 1998, **10**, 734.
- 41 R. Y. Mahale, A. Arulkashmir, K. Dutta and K. Krishnamoorthy, *Phys. Chem. Chem. Phys.*, 2012, **14**, 4577.
- 42 C. P. Chen, S. H. Chan, T. C. Chao, C. Ting and B. T. Ko, *J. Am. Chem. Soc.*, 2008, **130**, 12828.
- 43 R. C. Hiorns, R. de Bettignies, J. Leroy, S. Bailly, M. Firon, C. Sentein, H. Preud'homme and C. DagronLartigau, *Eur. Phys. J.-Appl. Phys.*, 2006, **36**, 295.
- 44 P. Schilinsky, U. Asawapirom, U. Scherf, M. Biele and C. J. Brabec, *Chem. Mater.*, 2005, **17**, 2175.
- 45 A. C. Mayer, S. R. Scully, B. E. Hardin, M. W. Rowell and M. D. McGehee, *Mater. Today*, 2007, **10**, 28.
- 46 S. R. Scully and M. D. McGehee, *J. Appl. Phys.*, 2006, **100**, 034907.
- 47 W. W. Li, Y. Han, Y. L. Chen, C. H. Li, B. S. Li and Z. S. Bo, *Macromol. Chem. Phys.*, 2010, **211**, 948.
- 48 C. P. Chen, Y. C. Chen and C. Y. Yu, *Polym. Chem.*, 2013, **4**, 1161.
- 49 C. Y. Li, T. C. Wen, T. H. Lee, T. F. Guo, J. C. A. Huang, Y. C. Lin and Y. J. Hsu, *J. Mater. Chem.*, 2009, **19**, 1643.
- 50 S. Chen, C. E. Small, C. M. Amb, J. Subbiah, T. H. Lai, S. W. Tsang, J. R. Manders, J. R. Reynolds and F. So, *Adv. Energy Mater.*, 2012, **2**, 1333.
- 51 Z. Tan, D. Qian, W. Zhang, L. Li, Y. Ding, Q. Xu, F. Wang and Y. Li, *J. Mater. Chem. A*, 2013, **1**, 657.
- 52 H. L. Yip and A. K. Y. Jen, *Energy Environ. Sci.*, 2012, **5**, 5994.
- 53 M. Manceau, E. Bundgaard, J. E. Carlé, O. Hagemann, M. Helgesen, R. Søndergaard, M. Jørgensen and F. C. Krebs, *J. Mater. Chem.*, 2011, **21**, 4132.

Organic/Metallic Nanohybrids Based on Amphiphilic Dumbbell-Shaped Dendrimers

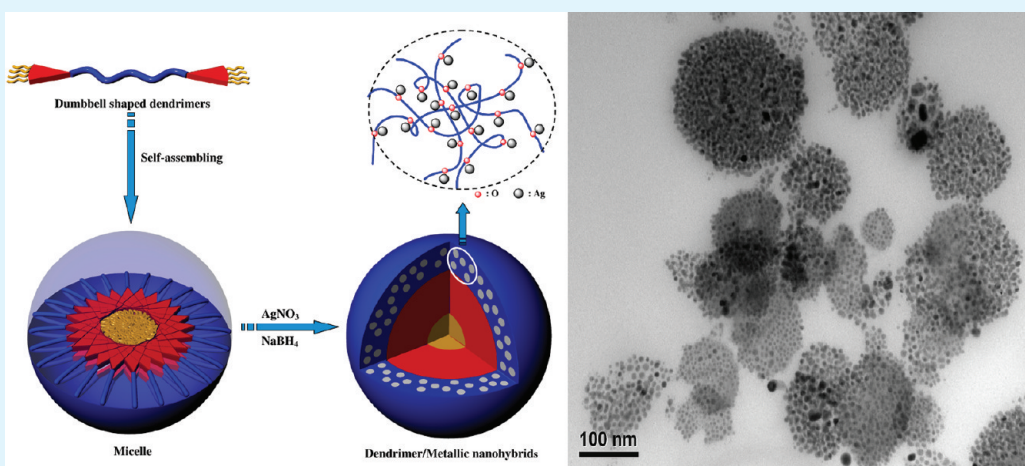
Shi-Min Shau,[†] Chia-Cheng Chang,[†] Chia-Hao Lo,[†] Yi-Chu Chen,[†] Tzong-Yuan Juang,[‡] Shenghong A. Dai,[†] Rong-Ho Lee,^{*,†} and Ru-Jong Jeng^{*,†,§}

[†]Department of Chemical Engineering, National Chung Hsing University, Taichung 402, Taiwan

[‡]Department of Applied Chemistry, National Chiayi University, Chiayi 60004, Taiwan

[§]Institute of Polymer Science and Engineering, National Taiwan University, Taipei 10617, Taiwan

S Supporting Information



ABSTRACT: In this study, we synthesized a series of amphiphilic dumbbell-shaped dendrimers through the addition reactions of a hydrophilic poly(oxyalkylene) with hydrophobic dendrons based on 4-isocyanate-4'-(3,3-dimethyl-2,4-dioxo-azetidine)-diphenylmethane with different numbers of branching generations. The addition reaction of azetidine-2,4-diones of dendrons to amines of poly(oxyalkylene) was proceeded by stirring the reactants in dry tetrahydrofuran (THF) under nitrogen at 60 °C. In aqueous media, the dumbbell-shaped dendrimers self-assembled into micelles with their hydrophobic dendrons in the core and their hydrophilic poly(oxyalkylene) segments forming loops in the corona shell. Employing the unique self-assembled micelle structures as templates for subsequent chemical reduction of the Ag^+ ions, we generated new types of organic/metallic [silver nanoparticle (AgNP)] nanohybrid clusters. The long poly(oxyalkylene) loops that extended into the aqueous phase complexed with the Ag^+ ions, providing the suspension with steric stabilization to prevent the AgNPs from collision and flocculation. After reduction, the AgNPs were present in a homogeneous distribution in the round dendrimer micelle-stabilized nanoclusters. The diameter of each AgNP was less than 10 nm; the diameter of each round nanocluster was in the range of 50–200 nm. The encapsulation efficiency of the AgNPs in micelles was about 54–69% for the dumbbell-shaped dendrimer based organic/AgNP nanohybrid.

KEYWORDS: dendron, dumbbell-shaped dendrimer, self-assembly, silver nanoparticle

INTRODUCTION

The self-assembly of low-molecular-weight amphiphiles,¹ linear block copolymers,^{2–4} dendrimers,⁵ dendronized polymers,^{6,7} and hyper-branched polymers^{8–11} with well-defined molecular structures continues to attract much attention. Molecular self-assembly is a spontaneous process in which molecules form ordered nanostructures mediated by noncovalent driving forces, typically Coulombic electrostatic interactions, van der Waals forces, π - π stacking interactions, hydrogen bonding, ion-exchange, and ionic adsorption.^{12–15} Combinations of solution self-assembly, interfacial self-assembly, and hybrid self-assembly

processes have led to the preparation of many elaborate nanoscopic supramolecular materials, including nano- and micro-scale spherical micelles and vesicles, cylindrical tubules and fibers, and monolayer and multilayer arrays.^{16–19} The preparation of such nanoscopic materials has been a major research area in nanoscience and -engineering. Especially, the dendritic macromolecules with specific nanostructures exhibit

Received: September 15, 2011

Accepted: March 27, 2012

Published: March 27, 2012

promising applications in fields ranging from green chemistry,²⁰ biochemistry,^{21–28} and opto-electronics²⁹ to nanotechnology.^{30,31}

The dendritic macromolecules possess highly branched, globular geometric shapes and an exponentially increasing number of terminal groups. Because of this, dyes, drugs, and metal ions were encapsulated by the terminal groups through ligand chelation, hydrogen bonding interaction, or electrostatic adsorption.^{21,23,32} Moreover, amphiphilic dendrimers that could self-assemble in aqueous media to form hydrophobic micelle cores were applicable in encapsulation and drug delivery systems.^{21,22,24,25,33} In addition, the dendritic architectures of dendrimers were also used as gates and molecular gradients for the preparation of well dispersed metal nanoparticles (NPs) in polymer solutions.^{30,31} The growth of metal nanoclusters could be controlled during the formation of interdendrimer complexes, resulting in larger metal nanoclusters protected by the exterior functional groups of the dendrimers.^{30,31} The stabilization and assembly of these organic/metallic nanohybrids were attributed to either the metal particles being attached to the protecting polymers or the protecting molecules covering or encapsulating the metal NPs.^{30,31} In fact, the silver nanoparticles (AgNPs) have been prepared by the chemical reduction of the silver ions in linear polymer,^{34,35} comb-like copolymer,³⁶ or dendrimer solution.^{30,31} Apart from that, poly(ethylene oxide) (PEO) or polyethylene glycol (PEG) based dumbbell-shaped dendrimers have been reported for biomaterial applications.^{32,37–45} However, the PEO or PEG based dumbbell-shaped dendrimers have not been used as the surfactant for the preparation of the homogeneously distributed AgNP aqueous solution. It is important to note that the preparation of the AgNPs through the chemical reduction of silver ions in micelles has not been reported.

Recently, we synthesized a series of polyurea/malonamide dendrons using 4-isocyanato-4'-(3,3-dimethyl-2,4-dioxoazetidino)diphenylmethane (IDD) as a building block.⁴⁶ Our synthetic approach toward the polyurea/malonamide dendrons, consisting of alternating addition reactions to the isocyanate and azetidine-2,4-dione groups of IDD, allowed the rapid and selective synthesis of dendrons without the need for traditional protection or activation chemistry. Such dendrons containing hydrogen bond-rich malonamide linkages along with long alkyl chains at their peripheries have served as surfactants for the surface modification of montmorillonite.^{47,48} The azetidine-2,4-dione functional group of IDD undergoes ring-opening reactions with aliphatic primary amines to form malonamide linkages.⁴⁸ In order to prepare a well dispersed AgNP in micelle solution, we designed and synthesized a series of novel dumbbell-shaped dendrimers based on IDD and PEO. A two-step approach was taken to prepare these dumbbell-shaped dendrimers for the dendron synthesis, we selected IDD as the building block to prepare dendrons via a convergent route; for the synthesis of the dumbbell-shaped dendrimers, we employed hydrophilic PEO (Jeffamine ED-2003) as the coupling agent for selective ring-opening additions of azetidine-2,4-dione units. In addition, the dumbbell-shaped dendrimer based oil-in-water (O/W) micelles were prepared using a cosolvent method.^{2,49} The surface tension measurements were used to evaluate the concentrations of micelles of the dumbbell-shaped dendrimers. Moreover, we employed atomic force microscopy (AFM) and transmission electron microscopy (TEM) to characterize the morphologies of the micelles derived from the dumbbell-shaped dendrimers. The morphologies obtained after the self-assembly of amphiphilic dendritic macromolecules are

influenced by the chemical structures and the processing conditions (e.g., solution concentration, temperature, pH, and medium). After loading Ag⁺ ions into the self-assembled supramolecules, followed by chemical reduction, we obtained a new type of organic/silver nanoparticle (AgNP) nanohybrid. We examined the effects of various relevant parameters on the sizes and shapes of these organic/AgNP nanohybrids. More importantly, better dispersion of AgNPs in micelles was achieved as compared to the ones prepared in the medium without the presence of micelles.

■ EXPERIMENTAL SECTION

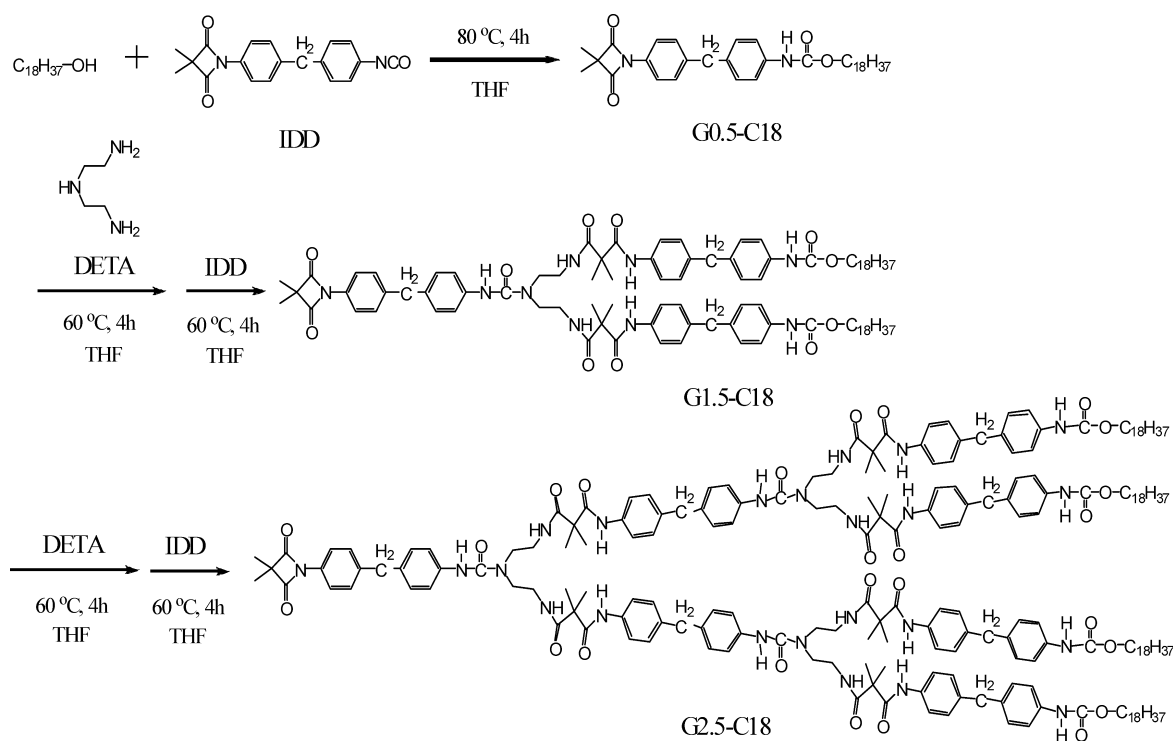
Materials. Isobutryl chloride, triethylamine (TEA), diethyltri-amine (DETA), stearyl alcohol (C18-OH; purity = 97.0%), and PEO Jeffamine XTJ-502 (ED-2003) ($M_w = 2000$ kg/mol) were purchased from Sigma–Aldrich. All chemicals were purchased and used as received, unless otherwise stated. *N,N*-Dimethylacetamide (DMAc) was purchased from Tedia, distilled over CaH₂, and then stored over 4-Å molecular sieves. Tetrahydrofuran (THF, Tedia) was distilled over Na/benzophenone under a N₂ atmosphere prior to use. Scheme 1 displays the chemical structures of the stearyl group–functionalized IDD derivatives featuring different numbers of branched generation dendrons (from G0.5-C18 to G2.5-C18). The building block IDD and the dendrons (from G0.5-C18 to G2.5-C18) were synthesized according to previous reports.^{46–48,50–54} Scheme 2 presents the synthetic route toward the amphiphilic dumbbell-shaped dendrimers. The dumbbell-shaped dendrimers (D-G0.5-C18, D-G1.5-C18, and D-G2.5-C18) were synthesized through the end-capping of ED-2003 with dendrons having different branched generations (G0.5-C18, G1.5-C18, G2.5-C18).^{48,55}

Dumbbell-Shaped Dendrimer D-G0.5-C18. A solution of G0.5-C18 (0.6 g, 1.0 mmol) and ED-2003 (1.0 g, 0.5 mmol) in dry THF (15 mL) was stirred at 60 °C under a N₂ atmosphere for approximately 4 h. After cooling to room temperature, the volatiles were evaporated under reduced pressure. The crude product was purified through column chromatography (SiO₂; EtOAc/hexanes) to obtain D-G0.5-C18 as a yellowish viscous liquid (0.50 g, 35%). $M_n = 4590$ g mol⁻¹; PDI = 1.09. ¹H NMR (400 MHz, DMSO): δ 0.70–0.92 (t, 6H, CH₃), 0.93–1.50 [br, 81H, CH₂, OC(CH₃)C, OCC(CH₃)], 1.30–1.40 [s, 12H, C(CH₃)₂], 1.40–1.50 (m, 4H, OCH₂C), 3.0–3.7 (br, 176H, OCH₂CH₂, OCHCH₂, OCH₂CH), 3.78–3.94 (s, 4H, ArCH₂Ar), 3.95–4.15 (t, 4H, COOCH₂), 6.90–6.71 (d, 4H, ArH), 7.10–7.30 (d, 8H, ArH), 7.35–7.45 (d, 4H, ArH). FTIR: ν_{\max} 3313 (NH), 1656 [C=O(NH)] cm⁻¹. Anal. Calcd. for C₁₇₃H₃₀₃N₆O₃₃: C, 62.81%; H, 9.18%; N, 2.54%; O, 25.60%. Found: C, 63.12%; H, 8.95%; N, 2.61%; O, 25.30%.

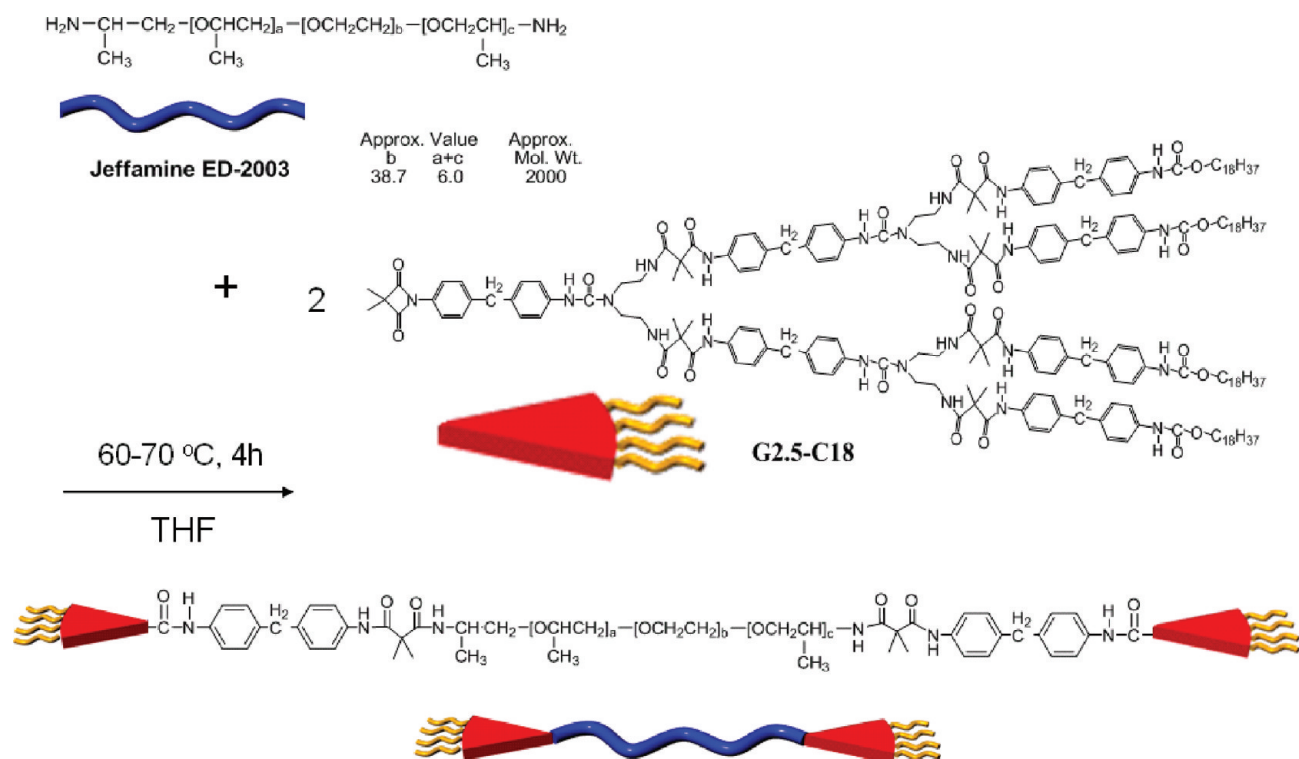
Dumbbell-Shaped Dendrimer D-G1.5-C18. D-G1.5-C18 was synthesized, using the same procedure as that described above for D-G0.5-C18, as a yellowish solid (0.81 g, 30%). $M_n = 5990$ g mol⁻¹; PDI = 1.04. ¹H NMR (400 MHz, DMSO): δ 0.78–0.91 (t, 12H, CH₃), 1.10–1.30 [br, 177 H, CH₂, OC(CH₃)C, OCC(CH₃), C(C₂H₆-CON)], 1.43–1.70 (m, 8H, OCH₂C), 3.10–3.60 (br, 208 H, OCH₂CH₂, OCHCH₂, OCH₂CH, CONHAr), 3.70–3.90 (s, 8H, ArCH₂Ar), 3.90–4.10 (t, 8H, COOCH₂), 7.00–7.20 (d, 8H, ArH), 7.20–7.40 (d, 16H, ArH), 7.40–7.60 (d, 8H, ArH), 7.82–8.00 (b, 4H, NH), 8.40–8.60 (s, 2H, NH), 9.20–9.40 (b, 4H, NH), 9.40–9.60 (br, 4H, NH). FTIR: ν_{\max} 3312 (NH), 1659 [C=O(NH)] cm⁻¹. Anal. Calcd. for C₂₉₃H₄₆₉N₂₀O₆₇: C, 65.89%; H, 8.79%; N, 5.25%; O, 20.10%. Found: C, 65.90%; H, 8.60%; N, 5.21%; O, 19.80%.

Dumbbell-Shaped Dendrimer D-G2.5-C18. D-G2.5-C18 was synthesized, using the same procedure as that described above for D-G0.5-C18, as a yellowish solid (0.62 g, 25%). $M_n = 7453$ g mol⁻¹; PDI = 1.11. ¹H NMR (400 MHz, DMSO): δ 0.78–0.90 (t, 24H, CH₃), 0.90–1.40 [br, 345 H, CH₂, OC(CH₃)C, OCC(CH₃), C(C₂H₆-CON)], 1.40–1.63 (m, 16H, OCH₂C), 3.10–3.60 (br, 224 H, OCH₂CH₂, OCHCH₂, OCH₂CH, CONHAr), 3.70–3.90 (s, 28H, ArCH₂Ar), 3.90–4.10 (t, 16H, COOCH₂), 6.90–7.20 (d, 28H, ArH), 7.30–7.60 (d, 84H, ArH), 7.820–8.0 (b, 16H, NH), 8.40–8.60

Scheme 1. Synthesis of Dendrons from Building Block IDD



Scheme 2. Synthesis of Dumbbell-Shaped Dendrimers



Dumbbell shaped dendrimers

(s, 10H, NH), 9.20–9.40 (b, 20H, NH), 9.40–9.60 (b, 20H, NH). FTIR: ν_{max} 3316 (NH), 1654 [C=O(NH)] cm^{-1} . Anal. Calcd. for $C_{533}H_{831}N_{48}O_{95}$: C, 67.90%; H, 8.81%; N, 7.13%; O, 16.13%. Found: C, 67.85%; H, 8.21%; N, 7.05%; O, 16.07%.

Micelles Derived from Self-Assembly of Dendrimers. To study the self-assembly behavior of micelles based on amphiphilic dumbbell-shaped dendrimers, dendrimer based oil-in-water (O/W) micelles were prepared using a cosolvent method.^{2,49} This is due to the

fact that better solubility was observed for the dendrimer in a mixed solvent (THF/water) than in the pure water.⁵⁶ For the dumbbell-shaped dendrimers (D-G0.5-C18, D-G1.5-C18, D-G2.5-C18), gelation and precipitation occurred when directly added to water. No micelle was formed in the pure water. On the other hand, a solution of a dumbbell-shaped dendrimer in THF was added slowly into vigorously stirred deionized water such that the final THF/water ratio was 1:50 (v/v). Micelles based on the dumbbell-shaped dendrimer were formed in solutions containing various contents of the dendrimer (10^{-2} , 10^{-3} , 10^{-4} , 10^{-5} , and 10^{-6} wt %). To study the self-assembly behavior of micelles on the plates of glass cells, solutions with various micelle concentrations were placed into glass cells and left to allow the solvent to evaporate, thereby inducing the self-assembly of the micelles on the glass cell plates.

AgNP Dispersal in Micelles of Dumbbell-Shaped Dendrimers. Silver nitrate (AgNO_3) was added [at various AgNO_3 -to-dendrimer mole ratios (from 1 to 100 000)] to an aqueous solution containing micelles of a dumbbell-shaped dendrimer. Furthermore, four equivalents of reduction agent NaBH_4 were added to the solution with vigorous stirring. During the reduction process, the color of solution changed from transparent to yellowish, indicating that reduction of Ag^+ to Ag^0 was occurring in the micelle solution. The UV-vis absorption spectrum of the AgNP-dispersed micelle solution was measured to evaluate the reduction of the Ag colloid in solution. In addition, the encapsulation capacity of the AgNPs in the dumbbell-shaped dendrimer based micelles was calculated according to the literature.¹¹ The organic/AgNP nanohybrid solution was prepared by the reduction of the AgNO_3 ($\text{AgNO}_3/\text{D-G2.5-C18}$ molar ratio: 1000:1) in the dumbbell-shaped dendrimer based micelle (10^{-4} wt %, 1.34×10^{-7} M) solution. The organic/AgNP nanohybrid solution was then dialyzed against deionized water with a dialysis membrane (molecular weight cut off: 12 000–14 000 g/mol) for 24 h. The encapsulation efficiency of the AgNPs in the dumbbell-shaped dendrimer based micelles was calculated by measuring the absorption intensity of AgNPs at 389 nm before and after the dialysis of the aqueous solution of the dumbbell-shaped dendrimer based organic/AgNP nanohybrid.¹¹ The encapsulation efficiency of AgNPs in the dendrimer based micelles was calculated as follows:

$$\frac{I_{\text{UV absorbance after dialysis}}}{I_{\text{UV absorbance before dialysis}}} \times 100\%$$

Measurements. ^1H NMR spectra were recorded using a Varian Gemini-400 (400 MHz). Fourier transform infrared (FTIR) spectra were recorded using a PerkinElmer Spectrum spectrometer. Ultraviolet-visible (UV-vis) spectra were recorded using a Shimadzu UV-1240 spectrometer. Differential scanning calorimetry (DSC) and thermogravimetric analysis (TGA) were performed using a Seiko SSC-5200 apparatus operated at a heating rate of $10^\circ\text{C}/\text{min}$ under a N_2 atmosphere. The thermal degradation temperature (T_d) was taken to be the temperature at which 5% weight loss occurred. Gel permeation chromatography (GPC) was performed using a Waters chromatography system (Waters, 717 plus Autosampler), two Waters Styragel linear columns, polystyrene as the standard, and THF as the eluent. Elemental analysis was performed using a Heraeus CHN-OS Rapid Analyzer. The surface tension was measured using a FTA100 tensiometer and the pendant drop method. The critical micelle concentrations (CMCs) were the transition points obtained through extrapolation of the surfactant concentrations plotted with respect to the surface tension. X-ray diffraction (XRD) analysis was performed using a 3-kW Rigaku III diffractometer with a Cu target ($\lambda = 1.542 \text{ \AA}$), operated at a scanning rate of $2^\circ/\text{min}$. The d spacing of the sample was analyzed using Bragg's equation ($n\lambda = 2d \sin \theta$). Transmission electron microscopy (TEM) was performed using a Zeiss EM 902A instrument operated at 120 kV. Scanning electron microscopy (SEM) images were recorded using a Hitachi S-5200 field-emission scanning electron microscope after sputtering the films with a thin layer of Au/Pt alloy. Atomic force microscopy (AFM) images were recorded under ambient conditions using a Seiko SPI3800N Series SPA-400 operated in the tapping mode. The particle size and distribution of micelles in solution were estimated using a dynamic laser light scattering particle size

analyzer (90 Plus Brookhaven Instrument Corp.) equipped with a 15 mW solid-state laser (675 nm).

RESULTS AND DISCUSSION

Scheme 1 presents the route that we used to synthesize different branched generation dendrons (from G0.5-C18 to G2.5-C18) with peripheral octadecyl chains.^{46,47} The azetidine-2,4-dione functional group of IDD reacted only with aliphatic primary amino groups under the synthetic conditions employed herein. FTIR spectra of the dendrons indicated that the signals of the azetidine-2,4-dione units (1738 and 1856 cm^{-1}) disappeared, and a peak for the malonamide units appeared at 1675 cm^{-1} after the reaction between IDD and DETA. ^1H NMR spectra confirmed the chemical structures of the dendrons. The chemical shifts and relative intensities of the signals were in agreement with the proposed structures for these dendrons. As illustrated in Scheme 2, we synthesized the dumbbell-shaped dendrimers (dendron-coil-dendron; ABA-type) through end-capping ring-opening reactions of ED-2003 with the different branched generations of the azetidine-2,4-dione group-containing dendrons. ^1H NMR spectra confirmed the chemical structures of the dumbbell-shaped dendrimers (from D-G0.5-C18 to D-G2.5-C18); the chemical shifts and relative intensities of the signals (Figure 1) were in agreement with the proposed structures of these dendrimers. In addition, GPC provided valuable information confirming the purity of these dendrimers. Evolution of GPC traces (see the Supporting Information, Figure S1) shows that all dendrimers were one-peak distribution, confirming the absence of side products. Table 1 summarizes the average molecular weights of the starting ED-2003 and the dumbbell-shaped dendrimers. The molecular weights of the dumbbell-shaped dendrimers were closely related to their theoretical molecular weights, with polydispersities (PDI = 1.04–1.11) narrower than that of the starting material (ED-2003), indicating that their molecular sizes could be controlled to serve as an effective encapsulant for guest molecules.

Table 2 summarizes the TGA data of the dendrons and dumbbell-shaped dendrimers. The values of T_d (5% weight loss) of the dendrons G0.5-C18 to G2.5-C18 ranged from 250 to 278°C . Thermal properties of the dendrons were dependent on the degree of branching and the molecular weight. Dendrons with intermediate generations (G0.5-C18, G1.5-C18, G2.5-C18) exhibited higher thermal stabilities than the dendrons with integer generation (G1.0-C18, G2.0-C18). We attribute the lower values of T_d of the dendrons G1.0-C18 and G2.0-C18 to the presence of poor thermal stability of the exposed diethylamine units in the dendrons. Moreover, the values of T_d of the dendrons increased slightly upon increasing the molecular weight. In addition, the values of T_d of the dumbbell-shaped dendrimers (from D-G0.5-C18 to D-G2.5-C18) were all in the range of 181 – 252°C . It is important to note that the values of T_d of the dendrimers were lower than those of the dendrons, due to the molecular interactions between the dendritic moieties and ED-2003 segments. The molecular interaction resulted in the reduction of packing order and crystallinity of dendron based domains. Therefore, lower thermal stability was observed for the dendrimers as compared to that of the corresponding dendrons. Typically, dendrimers with higher molecular weights and higher degrees of branching dendrons exhibit higher values of T_d ; we found, however, that the value of T_d of D-G2.5-C18 was lower than that of D-G1.5-C18, indicating that the high content of stearyl groups decreased the thermal stability of this dendrimer.

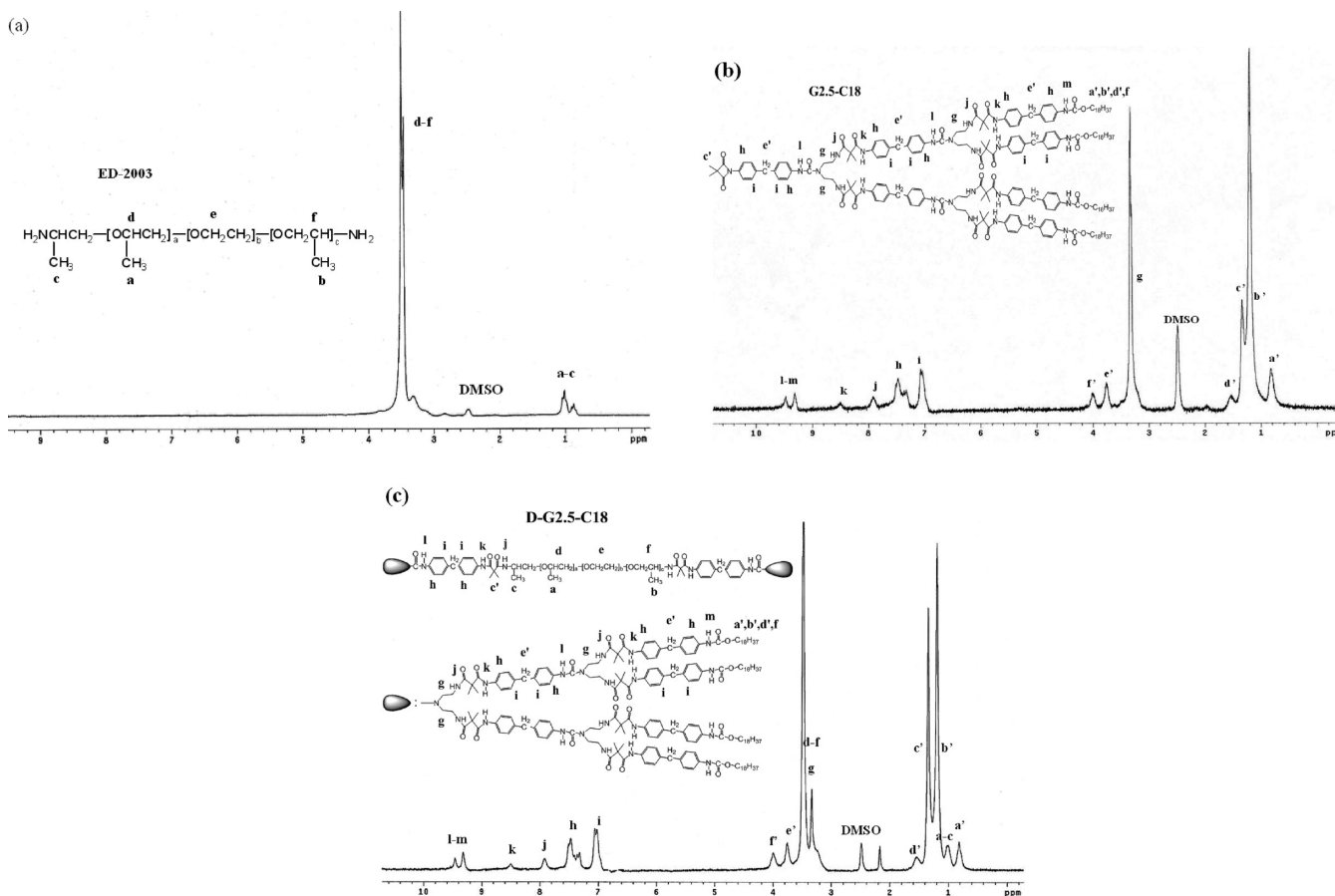


Figure 1. ^1H NMR spectra of (a) the ED-2003, (b) the dendron G2.5-C18, and (c) the dumbbell-shaped dendrimer D-G2.5-C18.

Table 1. Average Molecular Weights of the Dumbbell-Shaped Dendrimers^a

sample	M_n (g/mol)	M_w (g/mol)	PDI
ED-2003	2700	3200	1.18
D-G0.5-C18	4590	5005	1.09
D-G1.5-C18	5990	6217	1.04
D-G2.5-C18	7453	8298	1.11

^aDetermined through GPC analysis with THF as eluent (calibration: polystyrene standards).

Table 2. Thermal Properties of the Dendrons and Dumbbell-Shaped Dendrimers

sample	T_d^a (°C)	T_g^b (°C)	T_m^b (°C)
ED-2003	276	-65	27
G0.5-C18	272	- ^c	108
G1.0-C18	250	-	167
G1.5-C18	277	55	-
G2.0-C18	271	68	-
G2.5-C18	278	70	-
D-G0.5-C18	181	-	18/48
D-G1.5-C18	252	-	18/88
D-G2.5-C18	233	-	27/74

^aTemperature at which 5% weight loss occurred, recorded through TGA at a heating rate of 10 °C/min. ^bHeating rate of 10 °C/min under N_2 . ^cNot detectable.

Table 2 summarizes the glass transition temperatures (T_g) and melting points (T_m) of the dendrons and dendrimers.

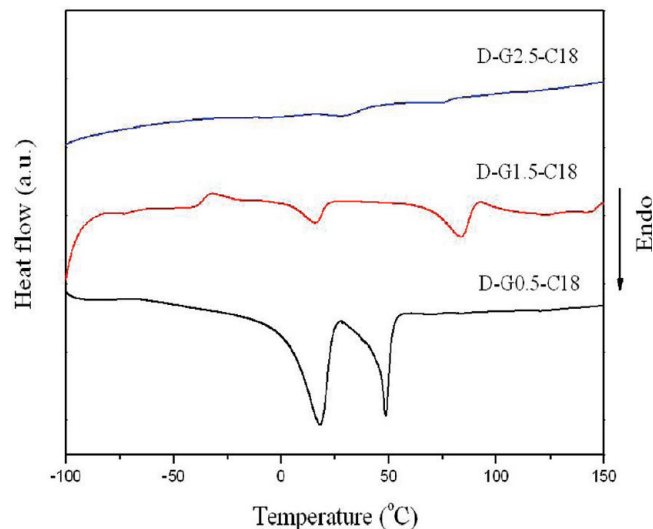


Figure 2. DSC thermograms of the dumbbell-shaped dendrimers.

According to the DSC thermograms, the dendrons G0.5-C18 and G1.0-C18 exhibited values of T_m of 108 and 167 °C, while the dendrons G1.5-C18, G2.0-C18, and G2.5-C18 possessed values of T_g of 55, 68, and 70 °C, respectively. We observed a crystalline phase for the dendron with the lower branching generation but amorphous phases for the dendrons of higher branching generation. Moreover, the value of T_g of the dendrons increased upon increasing the molecular weight and generation.^{30,31} Figure 2 displays the DSC thermograms of the

dumbbell-shaped dendrimers D-G0.5-C18 to D-G2.5-C18. Because the dendrimers comprised soft (ED-2003) and hard (dendron) blocks, all of the dumbbell-shaped dendrimers displayed two values of T_m pertaining to the partial micro-separation of poly(oxyalkylene) and dendron based domains, respectively. The lower value of T_m of the dendrimer was assigned to the ED-2003 based domains because the value of T_m of ED-2003 was as low as 27 °C. The values of T_m corresponding to the ED-2003 based domains in the dendrimers D-G0.5-C18, D-G1.5-C18, and D-G2.5-C18 were 18, 18, and 27 °C, respectively. The exothermic heat of T_m decreased upon increasing the branching generation of the dendrons in the dendrimers, revealing that the crystal capacity with respect to the ED-2003 based domains decreased upon the incorporation of the dendrons. The presence of the dendrons limited the molecular motion of the ED-2003 chains required for crystal organization. The chain mobility of ED-2003 would be restricted further by the presence of more highly branched generations of dendron. On the other hand, the values of T_m corresponding to the dendron based crystal domains of the dendrimers D-G0.5-C18, D-G1.5-C18, and D-G2.5-C18 were 48, 88, and 74 °C, respectively. Relative to D-G1.5-C18, the higher content of stearyl groups led to the lower value of T_m of D-G2.5-C18. In addition, as revealed in Figure 2, the exothermic heat of the melting transitions corresponding to the dendron based domains decreased upon increasing the branching generation of the dendrons. Thus, a high branching generation did not favor the formation of crystal domains of the dendrimers.

Table 3 lists the solubilities of the stearyl group-containing dendrons and dumbbell-shaped dendrimers in common organic

Table 3. Solubility Behavior of the Dendritic Compounds^a

sample	THF	acetone	MeOH	DMF ^b	DMAc ^b
G0.5-C18	++	+ -	--	++	++
G1.0-C18	--	--	--	++	++
G1.5-C18	++	+ -	--	++	++
G2.0-C18	+ -	--	--	++	++
G2.5-C18	++	+ -	--	++	++
D-G0.5-C18	++	++	+ -	++	++
D-G1.5-C18	++	++	--	++	++
D-G2.5-C18	++	++	--	++	++

^aSolubility determined from 10 mg of sample in 1 mL of solvent. ++: Soluble at room temperature. + -: Soluble after heating at 60 °C. --: Insoluble even after heating at 60 °C. ^bDMF: Dimethylformamide; DMAc: *N,N*-dimethylacetamide.

solvents, at a concentration of 10% (w/v). Each compound exhibited good solubility in polar solvents, especially in DMAc and dimethylformamide (DMF), because of the flexible alkyl chains at the periphery of the dendrons and the polar groups of the dendrimers, including the stearyl groups, urethane, and malonamide linkages. None of the samples was soluble in MeOH, even the dendrimers containing hydrophilic poly(oxyalkylene) segments. We attribute the partial solubility of the integer-generation dendrons G1.0-C18 and G-2.0-C18 in THF and acetone to the presence of the flexible or expansible diethylamine (CH₂CH₂NHCH₂CH₂) linker between the aromatic-rich building blocks, allowing the conformations of G1.0-C18 and G2.0-C18 to be more linear than those of the dendrons G0.5-C18, G-1.5-C18, and G-2.5-C18. Taken together, strong π - π stacking interactions between the aromatic building blocks, van der Waals forces between the long alkyl chains, and hydrogen bonding interactions

between the malonamide linkages decreased the solubility of the integer-generation dendrons G1.0-C18 and G2.0-C18.

To further monitor their intermolecular self-assembly behavior, the dendrons were dissolved in THF at various weight ratios (1, 10, and 20 wt %). We observed molecular aggregation and gelation only for the dendron G1.0-C18 in THF. The high branching dendron G2.0-C18 and its strong intramolecular interactions inhibited intermolecular aggregation, while the IDD units with kinked linkages inhibited the intermolecular aggregation and self-assembly of the dendrons G1.5-C18 and G2.5-C18. Therefore, gelation did not occur for the dendrons G1.5-C18, G2.0-C18, and G2.5-C18 in THF. Subsequently, we studied the molecular aggregation and gelation phenomena of the dendron G1.0-C18 in THF upon changing its concentration. As revealed in Figure 3,

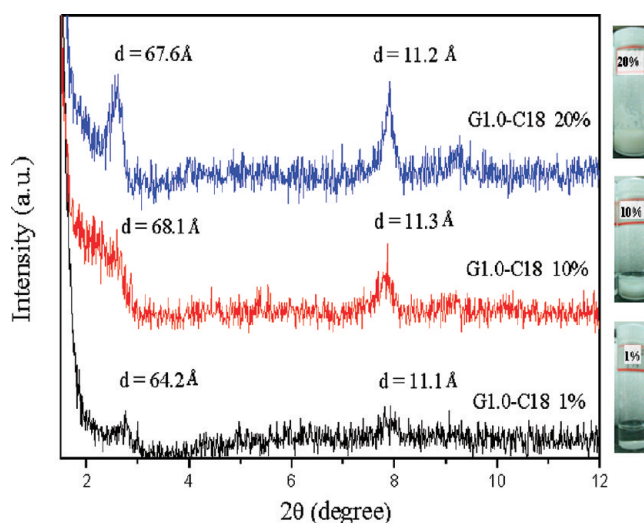


Figure 3. XRD patterns of the dried gels prepared from different weight percentages of G1.0-C18 in THF.

emulsion and gelation of the THF solution occurred when the concentration of dendron G1.0-C18 was greater than 10 wt %. We used XRD spectroscopy to further characterize the self-assembly behavior of the dendron G1.0-C18 in the gel state. Figure 3 indicates that only a high content of dendron G1.0-C18 (>5 wt %) in THF solution resulted in a gelation state. After drying the gel solution under vacuum, the XRD patterns of dried gels prepared from different concentrations of G1.0-C18 in THF revealed that the dendron molecules were integrated into regular nanostructures stabilized through strong intermolecular interactions. Two diffraction peaks with d spacings of 64–68 and 11 Å were evident in the spectra. Similar results have been reported for hydrogen bond-rich alkyl bis-acylurea derivatives;⁵⁷ their XRD patterns also provided evidence of 2D regular molecular packing in the organogel state. As illustrated in Figure 4, we propose that G1.0-C18 molecules self-assembled into multilayer structures, mediated by hydrogen bonds between the extended dendron molecules. The thickness of the layers of extended molecules was approximately that of the value of the d spacing (64–68 Å). On the other hand, we observed good solubility for the dumbbell-shaped dendrimers D-G0.5-C18 to D-G2.5-C18 in THF. Gelation did not occur for these dendrimers in THF, even though the dendron G1.0-C18 readily self-assembled into regular nanostructures through strong intermolecular interactions. Only a few dendrimers have been reported to exhibit well-defined mesophase behavior.¹⁹ The ability of a dendrimer

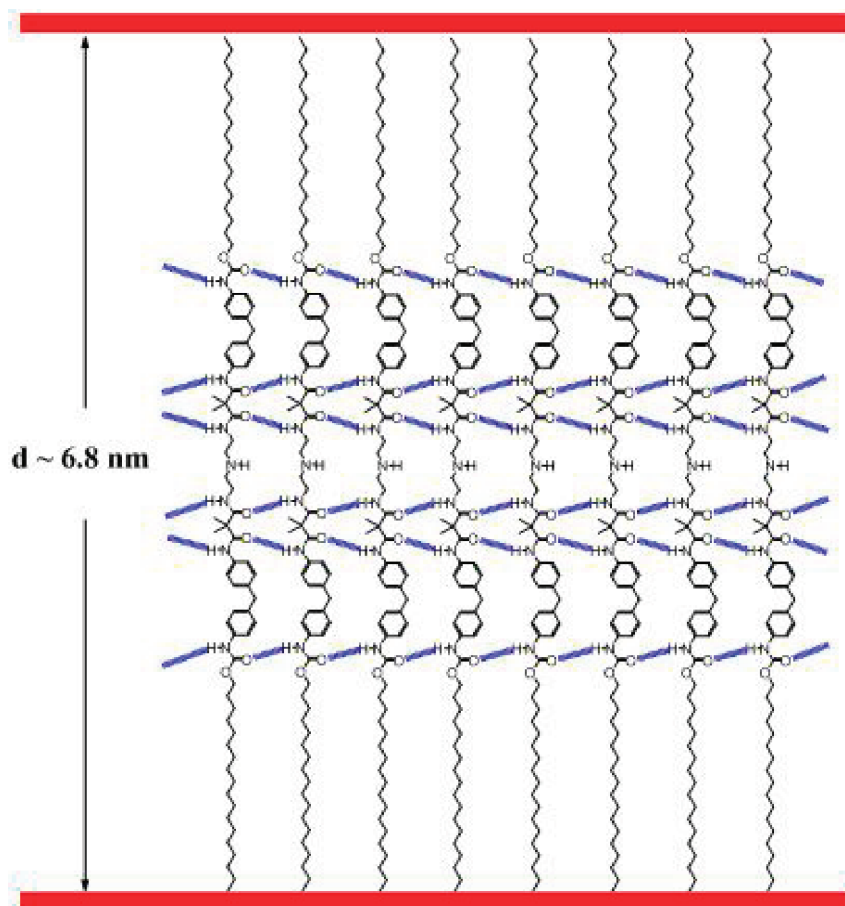


Figure 4. Schematic representation of the self-assembled lamellar structure formed from the dendron G1.0-C18.

to self-assemble is related to the shapes of its dendrons, the volume fractions of its hydrophilic and hydrophobic moieties, and the packing density of the dendritic structures.

We investigated the hydrophilic/hydrophobic balance, micellization behavior, and assembly behavior of the dendrimers with respect to their ability to decrease the surface tension of water. Figure 5 presents the concentration-dependent surface tension in the presence of the amphiphilic dumbbell-shaped dendrimers. In surface and colloid chemistry,

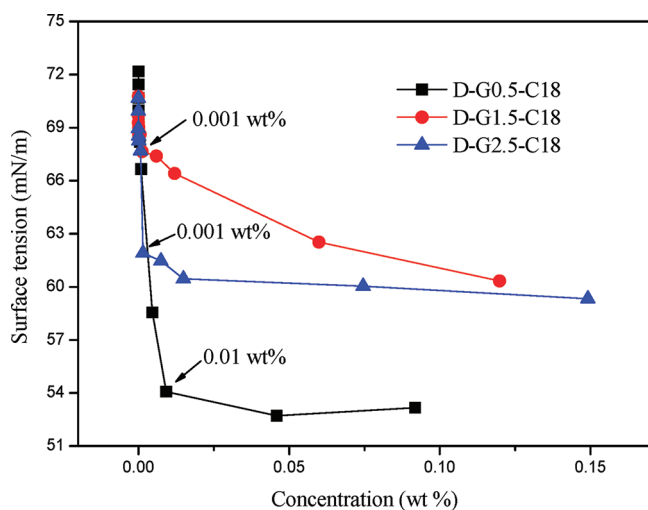


Figure 5. Surface tension as a function of concentration for the dumbbell-shaped dendrimers in aqueous solutions.

the CMC is the threshold concentration at which micellization begins; it appears as a discontinuity in the plot of the surface tension against the solution concentration. The experimental CMCs of our amphiphilic dumbbell-shaped dendrimers, determined from the turning points, ranged from 10^{-2} to 10^{-3} wt % (from ca. 2×10^{-5} to 2×10^{-6} M). The surface tension decreased from 72 to approximately 54–60 mN/m upon increasing the dendrimer content up to the CMC. The decrease in surface tension was more significant for the D-G0.5-C18 solution relative to those of the D-G1.5-C18 and D-G2.5-C18 solutions, presumably because the hydrophilicity of the dendron G0.5-C18 was greater than those of the dendrons G1.5-C18 and G2.5-C18. The hydrophilicity decreased upon increasing the contents of the building block IDD and the stearyl groups in the higher-generation dendrimers.

Compounds that form micelles are typically amphiphilic, meaning that they are soluble not only in protic solvents (e.g., water) in oil-in-water (O/W) systems but also in aprotic solvents as reverse micelles in water-in-oil (W/O) systems. A recent report suggested that spherical and relatively narrowly distributed micelles/vesicles are typically constructed through self-assembly of dendritic moieties and that they are more stable than the conventional ones obtained from linear blocks.^{29,44} In aqueous media, the dumbbell-shaped dendrimers will self-assemble into O/W micelles with their hydrophobic dendrons in the core and their hydrophilic poly(oxyalkylene) segments forming loops in the corona shell, on account of the favorable hydrophilic/hydrophobic balance. Conversely, water-induced reverse micelles in nonpolar solvents (e.g., toluene)

will exhibit reverse core/shell structures relative to the micelles. Figure 6 presents graphical representations of the structures of

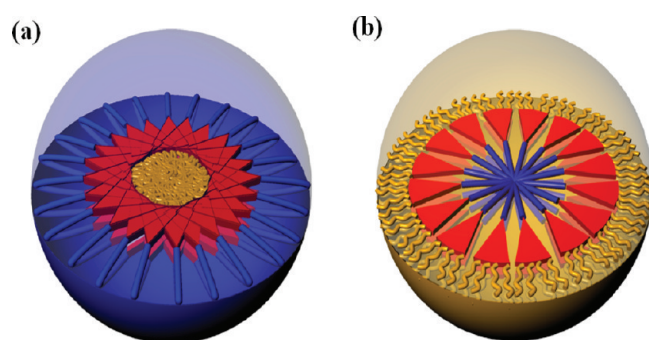


Figure 6. Schematic representations of (a) micelles and (b) reverse micelles formed from dumbbell-shaped dendrimers.

micelles and reverse micelles. Figure 7 presents SEM images of the dendrimer based micelles (10^{-4} wt %), indicating that the

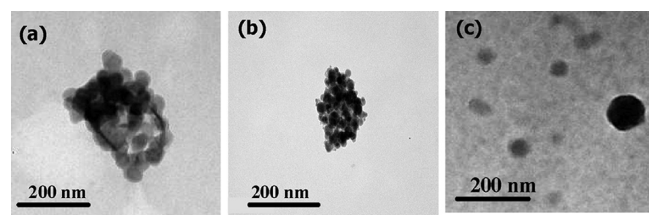


Figure 7. SEM images of micelles formed from the dendrimers (a) D-G0.5-C18, (b) D-G1.5-C18, and (c) D-G2.5-C18.

diameters of the micelles are in the range of 50–100 nm. The micelles of D-G2.5-C18 were distributed individually, while the agglomeration was observed for the micelles based on D-G0.5-C18 and D-G1.5-C18. The agglomeration of micelles implies that the micelles are not thermodynamically stable in aqueous solution. The suspension stability of micelles is related to the balance of the hydrophobicity and hydrophilicity of the dendrimer in aqueous solution. In order to investigate the dispersion of micelles in aqueous solution, the particle size and distribution of micelles were estimated using a dynamic laser light scattering particle size analyzer (as shown in Supporting Information, Figure S2). Two peak distributions of particle sizes were observed for the micelles based on D-0.5G-C18 (average size: 35 and 471 nm) and D-1.5G-C18 (average size: 60 and 614 nm), while the average particle size of D-2.5G-C18 based micelles with monodispersity was about 157 nm. The result is congruent with the observation of SEM images. The agglomeration of micelles led to two different particle size distributions for the D-0.5G-C18 and D-1.5G-C18 based micelles. On the other hand, the particle size peak distribution with monodispersity indicates that the D-2.5G-C18 based micelles exhibited excellent dispersion in aqueous solution. In addition, the particle size of the micelle was dependent on the volume fractions and molecular interactions of its hydrophilic and hydrophobic moieties.^{1,8,9,12,19,29,47} The average particle size of D-2.5G-C18 based micelles is larger than those of the micelles based on D-0.5G-C18 and D-1.5G-C18. The average particle size and distribution of dendrimer based micelles in aqueous solution play an important role for the preparation of organic/metallic nanohybrids.

The nano- to micrometer-scale secondary structures of aggregates (e.g., micelles, vesicles, fibers, ribbons, sheets) are dependent on the molecular structure, concentration, solvent solubility, and other solution variables (e.g., pH, ionic strength). Figure 8 presents a possible mechanism for the formation of

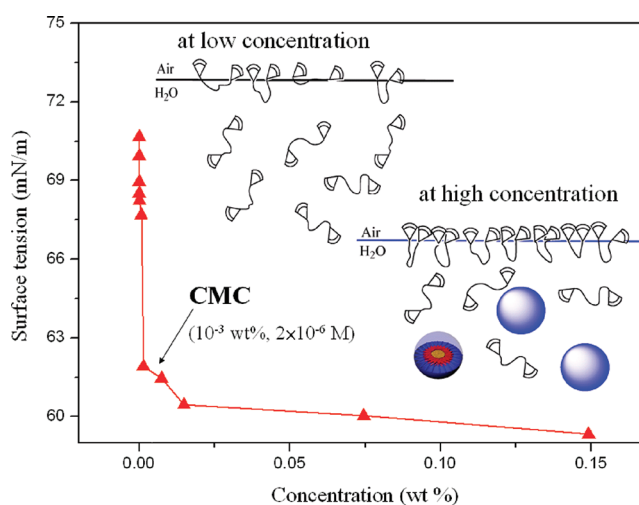


Figure 8. Surface tension as a function of concentration for D-G2.5-C18 in aqueous solution and schematic representation of micelle formation.

micelles from the amphiphilic dendrimer D-G2.5-C18 in aqueous solution. When the concentration of D-G2.5-C18 was less than CMC (ca. 10^{-3} wt %), the molecules of D-G2.5-C18 adsorbed and aggregated at the surface of the solution, thereby decreasing the surface tension; indeed, the surface tension decreased from 72 to approximately 60 mN/m upon increasing the concentration of D-G2.5-C18 in the aqueous solution up to CMC. Moreover, the molecules of D-G2.5-C18 could simply dissipate individually at the concentration below CMC and formed small aggregates or partially sank from the interface into the bulk of the aqueous solution when the concentration was close to CMC, at which point the adsorption of D-G2.5-C18 was saturated at the surface of the solution.⁵⁸ By definition, micelles will begin to form in a solution at CMC, the structures of which will depend on the structures of the amphiphilic molecules. When the concentration is greater than the CMC, these molecules spontaneously aggregate to form clusters (micelles), which result from physical interactions among the amphiphilic molecules rather than covalent bonding.

To further study the formation of micelles in aqueous solution, we prepared adsorbed D-G2.5-C18 substrates by dipping a glass plate into its solution for 24 h and then allowing the water to evaporate under ambient conditions. Figure 9a–d presents SEM images of the adsorbed substrates prepared from various concentrations of D-G2.5-C18 in aqueous solutions. When the concentration of D-G2.5-C18 in the aqueous solution was much less than CMC, only a few micelles formed in solution; the molecules of D-G2.5-C18 aggregated to form a colloidal material on the substrate (Figure 9a). When the concentration of D-G2.5-C18 increased to near CMC (10^{-4} wt %), symmetrical deformed (donut-shaped) micelles (outer diameter: 50–150 nm) formed on the glass plate (Figure 9b). It has been reported that the micelles with about 100 nm size were formed by the amphiphilic dumbbell-shaped dendrimers⁵⁹ and hyper-branched polymers.⁸ We attribute the deformation

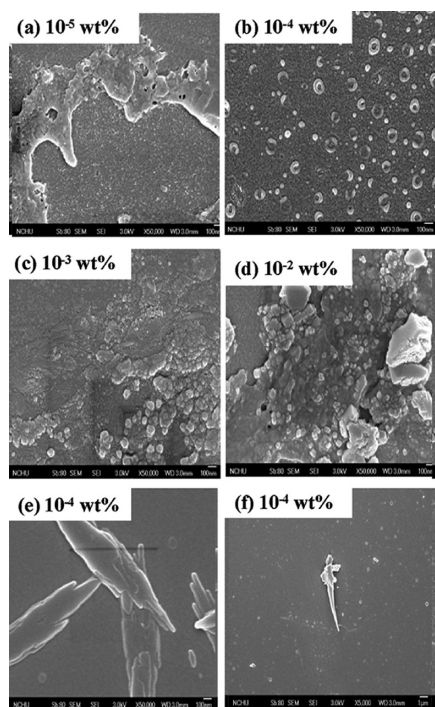


Figure 9. SEM images of micelles on glass plates, prepared from various concentrations of the dumbbell-shaped dendrimers (a–d) D-G2.5-C18, (e) D-G0.5-C18, and (f) D-G1.5-C18.

of the micelles to the collapse of hemispherical micelles on the glass plate upon evaporation of the water. Figure 10 provided a schematic illustration of the formation of D-G2.5-C18 based spherical micelles and their assembly on the substrate. Because of hydrophobic/hydrophilic balance, the center of each hemispherical micelle comprised mainly dendritic fragments (C18-dendron periphery). The formation of the donut shape was due to the lack of interpenetration and entanglement of the dendritic fragments in the middle of the hemispherical micelles.⁶⁰ As a result, donut-shaped micelles were formed on the substrate. This observation is consistent with the formation of micelles in aqueous solution. Furthermore, the micelle content increased with increasing concentration of D-G2.5-C18 in solution; as a result, aggregation of the micelles occurred on the substrate. As revealed in Figure 9c,d, greater degrees of adsorption of the micelle based clusters occurred on the

substrate for aqueous solutions containing higher concentrations of D-G2.5-C18 (10^{-2} and 10^{-3} wt %, respectively). In contrast, the dendrimers D-G0.5-C18 (Figure 9e) and D-G1.5-C18 (Figure 9f) did not form donut-shaped micelles on the glass plates. Bulk solid particles were formed on the glass plate for the dendrimers D-G0.5-C18 and D-G1.5-C18. The formation of bulk solid particles was presumably attributed to the high molecular interaction and agglomeration of the dendrimers on the glass plate.

Recently, poly(ethylene glycol)s of various chain lengths have been reported to play greater roles as stabilizers than as reducing agents for Ag^+ ions.⁶¹ The favorable complexation of ethoxy ($\text{CH}_2\text{CH}_2\text{O}$) groups with Ag^+ ions is well established.^{62,63} In each ethoxy-containing micelle colloid, we postulated that the hydrophobic dendrons were sequestered and solvated with THF in the core. Apart from that, the hydrophilic poly(oxyalkylene) loops were extended away from the center and bound to water molecules through hydrogen bonds. Therefore, we expected the corona exterior of the micelles, presenting poly(oxyalkylene) segment functionalities, to be capable of chelating Ag^+ ions and mediating their in situ reduction to form AgNPs. The long poly(oxyalkylene) loops extending into the aqueous phase and complexing the Ag^+ ions would provide suspension and steric stabilization to efficiently prevent the resulting AgNPs from collision and flocculation.

In aqueous solutions containing D-G2.5-C18 based micelles (10^{-4} wt %, 1.34×10^{-7} M), we used NaBH_4 as a reducing agent to transform various molar ratios of AgNO_3 into zero-valence AgNPs. During the reduction process, we confirmed the formation of micelle-stabilized AgNPs by observing color changes from colorless to yellowish, without precipitation. The yellow color of the colloidal sample (inset to Figure 11) is indicative of the presence of spherical AgNPs and the formation of Ag nanoclusters in solution. Furthermore, by varying the molar ratio of AgNO_3 to D-G2.5-C18 and monitoring the maximum UV–vis absorption of the solution, we established the reaction profile and optimal conditions for the transformation. Figure 11 presents the UV–vis spectra of the micelle-stabilized AgNPs prepared at various AgNO_3 /D-G2.5-C18 ratios. The maximum absorption appeared at a wavelength of 389 nm, corresponding to the dipole resonance of Ag nanospheres.^{56,64} The intensity of the absorption peak increased upon increasing the molar ratio of AgNO_3 to D-G2.5-C18. The absorption reached its maximum intensity

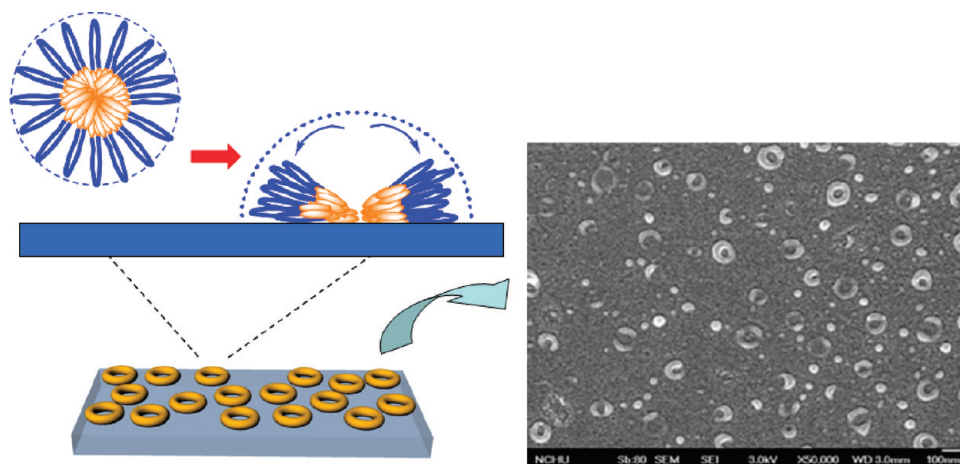


Figure 10. Schematic representation of spherical micelles assembled from the dendrimer D-G2.5-C18 on a substrate.

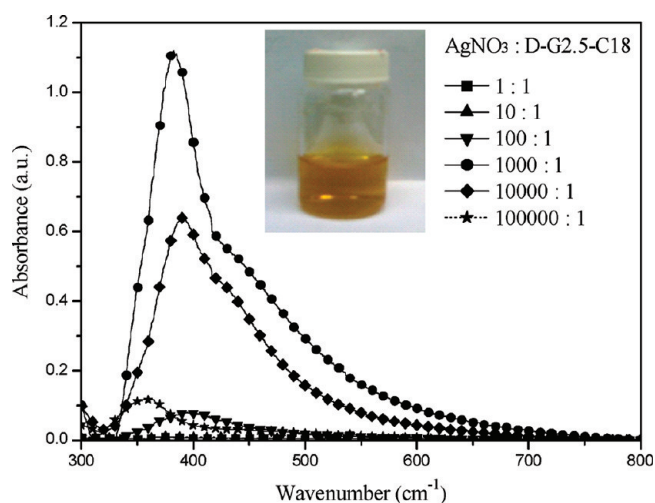


Figure 11. UV-vis spectra of micelle-stabilized AgNPs prepared at various $\text{AgNO}_3/\text{D-G2.5-C18}$ ratios; inset: photograph of the sample prepared at a $\text{AgNO}_3/\text{D-G2.5-C18}$ ratio of 1000:1.

when the $\text{AgNO}_3/\text{D-G2.5-C18}$ molar ratio was 1000:1, gradually decreasing thereafter up to a ratio of 10^5 because of the lower loading of D-G2.5-C18. In addition, the colloid based on the reduced $\text{AgNO}_3/\text{D-G2.5-C18}$ (molar ratio: 1000:1) system remained well dispersed in the aqueous solution. No aggregation of the Ag nanocomposite occurred in the colloid (inset to Figure 11).

Figure 12 provides a schematic representation of the self-assembly, with controllable particle size, of the AgNPs in the D-G2.5-C18 based micelles. After the addition of an appropriate amount of reducing agent, the AgNPs that formed were positioned initially between the extended poly(oxyalkylene) loops, but they gradually diffused into the dendron-rich core. SEM images reveal that the micelle particles had an average diameter of approximately 50–100 nm; TEM indicates that the average diameter of the spherical AgNPs was approximately 10–30 nm. Figure 13 presents TEM micrographs of the ED-

2003-stabilized and dendrimer (D-G0.5-C18 to D-G2.5-C18)-stabilized AgNPs. The AgNPs aggregated into large particles (average diameter: 20 nm) when we used ED-2003 as the template (Figure 13a); their dispersion was not uniform. We observed similar behavior for the D-G0.5-C18- and D-G1.5-C18-stabilized AgNPs (Figure 13b,c, respectively). We attribute the aggregation of these AgNPs to the agglomeration of micelles in the aqueous solutions containing D-G0.5-C18 and D-G1.5-C18. In contrast, the AgNPs obtained after reduction of the $\text{AgNO}_3/\text{D-G2.5-C18}$ micelles (Figure 13d) featured a homogeneous dispersion in the form of round nanoclusters; the average diameter of these AgNPs was much lower than 10 nm, while the average diameter of the round nanoclusters was approximately 50–200 nm. Almost all of the AgNPs were spherical. These results indicate that micelles of the amphiphilic dumbbell-shaped dendrimer D-G2.5-C18 were the more effective templates for hosting nanoclusters and stabilizing AgNPs to form unique organic/metallic nanohybrids. In addition to the distribution of AgNPs in the organic/AgNP nanohybrid, the encapsulation efficiency of the AgNPs in the micelles of dumbbell-shaped dendrimer was also investigated. The absorption intensity of AgNPs at 389 nm was reduced after the dialysis of the aqueous solution of the organic/AgNP nanohybrid (see the Supporting Information, Figure S3). According to the absorption intensity of AgNPs in the organic/AgNP nanohybrid, the encapsulation efficiencies of AgNPs were about 69.04, 56.48, and 54.07% for the micelles of D-G0.5-C18, D-G1.5-C18, and D-G2.5-C18, respectively. The encapsulation efficiency of AgNPs was closely related to the steric effect of the dendritic structure and the number of reduction groups of amines and oxyethylenes.^{31,34,36}

CONCLUSION

We have synthesized structurally symmetrical dendrimers (D-G0.5-C18 to D-G2.5-C18) featuring dendron-coil-dendron structures comprising an identical poly(oxyalkylene) middle block and different generation dendrons with peripheral octadecyl alkyl

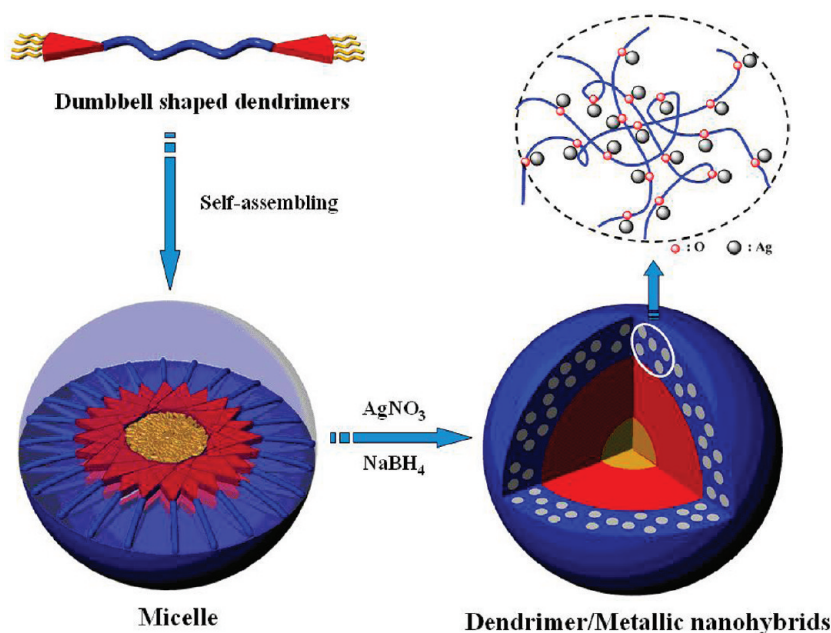


Figure 12. Schematic representation of micelle-stabilized AgNPs.

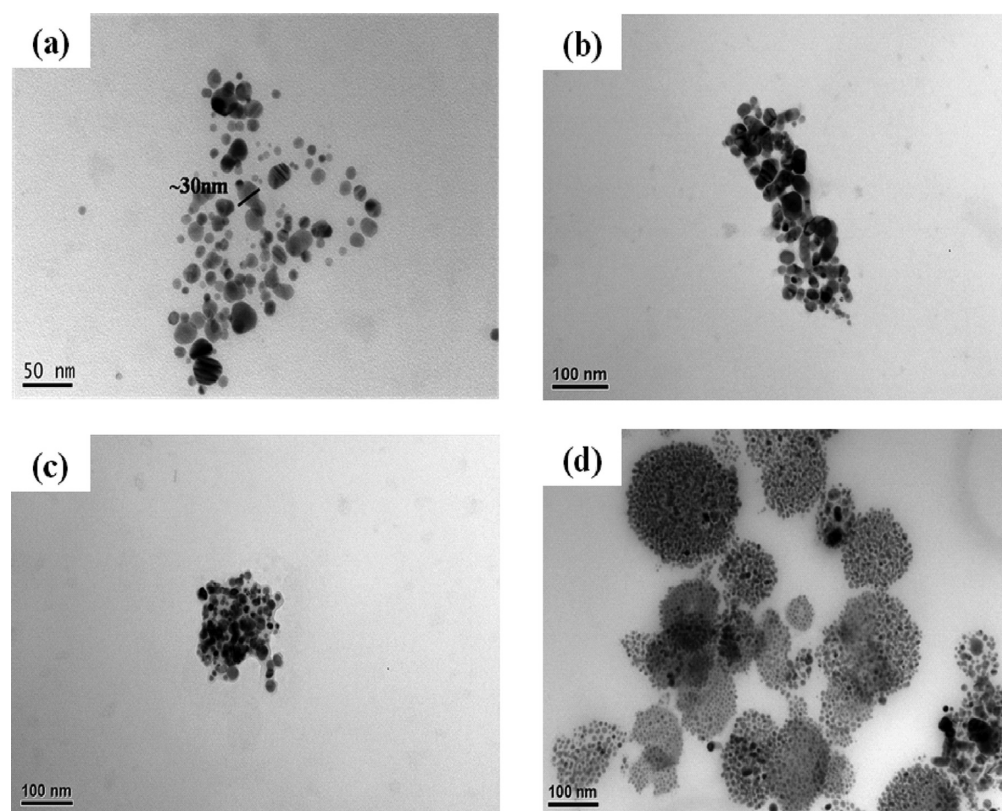


Figure 13. TEM micrographs of the micelle-stabilized AgNPs prepared using (a) ED-2003, (b) D-G0.5-C18, (c) D-G1.5-C18, and (d) D-G2.5-C18 as templates (10^{-4} wt % in aqueous solution).

chains. The thermal stability and solubility of these dendrimers was closely related to the generation of the dendrons. We observed a crystalline phase for the dendron with the lowest branching generation; the other dendrons with higher branching generations exhibited amorphous phases. A combination of strong π - π stacking between the aromatic building blocks, van der Waals forces between the long alkyl chains, and hydrogen bonding interactions between the malonamide linkages resulted in the lower solubility of the integer-generation dendrons. A correlation between the structure and surface tension revealed that the amphiphilic dumbbell-shaped dendrimer D-G2.5-C18 could self-assemble into micelles or large particles depending on its concentration in water. In aqueous media, the dumbbell-shaped dendrimers self-assembled into micelles with their hydrophobic dendrons in the core and their hydrophilic poly(oxyalkylene) segments forming the loops in the corona shell, on account of favorable hydrophilic/hydrophobic balance. SEM images revealed that the dendrimer D-G2.5-C18 was robust at forming micelles in aqueous media; these micelles, which featured hydrophobic cores surrounded by hydrophilic exterior poly(oxyalkylene) loops, were effective at stabilizing and assembling AgNPs to form organic/metallic nanohybrids. After the reduction of AgNO_3 , the AgNPs were distributed homogeneously in the dendrimer micelle-stabilized AgNP nanoclusters. High encapsulation efficiency of AgNPs was also observed for the dumbbell-shaped dendrimer based micelles.

■ ASSOCIATED CONTENT

Supporting Information

Figures of GPC traces of the dumbbell-shaped dendrimers and starting material PEO ED-2003, the particle size of the

dendrimer based micelles in aqueous solution, and the absorption intensity of AgNPs before and after dialysis of the aqueous solution of the dumbbell-shaped dendrimer based organic/AgNP nanohybrid. This material is available free of charge via the Internet at <http://pubs.acs.org>.

■ AUTHOR INFORMATION

Corresponding Author

*Tel.: +886-2-33665884. Fax: +886-2-33665237. E-mail: rhl@nchu.edu.tw (R.-H.L.); rujong@ntu.edu.tw (R.-J.J.).

Notes

The authors declare no competing financial interest.

■ ACKNOWLEDGMENTS

We thank the National Science Council of Taiwan for financial support.

■ REFERENCES

- (1) Estroff, L. A.; Hamilton, A. D. *Chem. Rev.* **2004**, *104*, 1201.
- (2) Zhang, W.; Shi, L.; An, Y.; Shen, X.; Guo, Y.; Gao, L.; Liu, Z.; He, B. *Langmuir* **2003**, *19*, 6026.
- (3) Di Cola, E.; Lefebvre, C.; Deffieux, A.; Narayanan, T.; Borsali, R. *Soft Matter* **2009**, *5*, 1081.
- (4) Riess, G. *Prog. Polym. Sci.* **2003**, *28*, 1107.
- (5) Percec, V.; Won, B. C.; Peterca, M.; Heiney, P. A. *J. Am. Chem. Soc.* **2007**, *129*, 11265.
- (6) Zhang, A. F.; Shu, L. J.; Bo, Z. S.; Schlüter, A. D. *Macromol. Chem. Phys.* **2003**, *204*, 328.
- (7) Kurzbach, D.; Kattinig, D. R.; Zhang, B.; Schlüter, A. D.; Hinderberger, D. *J. Phys. Chem. Lett.* **2011**, *2*, 1583.
- (8) Zhou, Y.; Yan, D. *Chem. Commun.* **2009**, 1172.
- (9) Zeng, F.; Zimmerman, S. C. *Chem. Rev.* **1997**, *97*, 1681.

- (10) Zhao, Y. H.; Xu, Y. Y.; Zhu, B. K. *Solid State Ionics* **2009**, *180*, 1517.
- (11) Zhang, L.; Hu, C. H.; Cheng, S. X.; Zhuo, R. X. *Colloids Surf., B: Biointerfaces* **2010**, *79*, 427.
- (12) Whitesides, G. M.; Grzybowski, B. A. *Science* **2002**, *295*, 2418.
- (13) Ho, R. H.; Chiang, Y. W.; Lin, S. S.; Chen, C. K. *Prog. Polym. Sci.* **2011**, *36*, 376.
- (14) Dawn, A.; Shiroki, T.; Haraguchi, S.; Tamaru, S. I.; Shinkai, S. *Chem. Asian J.* **2011**, *6*, 266.
- (15) Zhang, X.; Wang, C. *Chem. Soc. Rev.* **2011**, *40*, 94.
- (16) Kunitake, T.; Okahata, Y.; Shimomura, M.; Yasunami, S. I.; Takarabe, K. *J. Am. Chem. Soc.* **1981**, *103*, 5401.
- (17) Herr, D. J. C. *J. Mater. Res.* **2011**, *26*, 122.
- (18) Hamley, I. W. *Soft Matter* **2011**, *7*, 4122.
- (19) Cho, B. K.; Jain, A.; Gruner, S. M.; Wiesner, U. *Chem. Commun.* **2005**, 2143.
- (20) Simonyan, A.; Gitsov, I. *Langmuir* **2008**, *24*, 11431.
- (21) Aulenta, F.; Hayes, W.; Rannard, S. *Eur. Polym. J.* **2003**, *39*, 1741.
- (22) Liu, M.; Kono, K.; Fréchet, M. J. J. *Controlled Release* **2000**, *65*, 121.
- (23) Stiriba, S. E.; Frey, H.; Haag, R. *Angew. Chem., Int. Ed.* **2002**, *41*, 1329.
- (24) Weinhart, M.; Groger, D.; Enders, S.; Riese, S. B.; Dervedde, J.; Kainthan, R. K.; Brooks, D. E.; Haag, R. *Macromol. Biosci.* **2011**, *11*, 1088.
- (25) Papp, I.; Sieben, C.; Sission, A. L.; Kostka, J.; Bottcher, C.; Ludwig, K.; Herrmann, A.; Hang, R. *ChemBioChem* **2011**, *12*, 887.
- (26) Gillies, E. R.; Frechet, J. M. J. *J. Am. Chem. Soc.* **2002**, *124*, 14137.
- (27) Ihre, H. R.; Jesus, O. L. P. D.; Szoka, F. C.; Frechet, J. M. J. *Bioconjugate Chem.* **2002**, *13*, 443.
- (28) Gitsov, I.; Hamzik, J.; Ryan, J.; Simonyan, A.; Nakas, J. P.; Omori, S.; Krastanov, A.; Cohen, T.; Tanenbaum, S. W. *Biomacromolecules* **2008**, *9*, 804.
- (29) Xiong, W.; Wang, H.; Han, Y. *Macromol. Rapid Commun.* **2010**, *31*, 1886.
- (30) Sun, X.; Dong, S.; Wang, E. *Macromolecules* **2004**, *37*, 7105.
- (31) Kuo, P. L.; Chen, W. F. *J. Phys. Chem. B* **2003**, *107*, 11267.
- (32) Chapman, T. M.; Hillyer, G. L.; Mahan, E. J.; Shaffer, K. A. *J. Am. Chem. Soc.* **1994**, *116*, 11195.
- (33) Bronstein, L. M.; Shifrina, Z. B. *Chem. Rev.* **2011**, *111*, 5301.
- (34) Dong, R. X.; Tsai, W. C.; Lin, J. J. *Eur. Polym. J.* **2011**, *47*, 1383.
- (35) Chen, D. H.; Huang, Y. W. *J. Colloid Interface Sci.* **2002**, *255*, 299.
- (36) Hsu, Y. C.; Chen, Y. M.; Lin, W. L.; Lan, Y. F.; Chan, Y. N.; Lin, J. J. *J. Colloid Interface Sci.* **2010**, *352*, 81.
- (37) Gitsov, I.; Wooley, K. L.; Fréchet, J. M. J. *Angew. Chem., Int. Ed. Engl.* **1992**, *31*, 1200.
- (38) Gitsov, I.; Lambrych, K. R.; Remnant, V. A.; Pracitto, R. J. *Polym. Sci., Part A: Polym. Chem.* **2000**, *38*, 2711.
- (39) Gitsov, I.; Simonyan, A.; Vladimirov, N. G. *J. Polym. Sci., Part A: Polym. Chem.* **2007**, *45*, 5136.
- (40) Froimowicz, P.; Gandini, A.; Strumia, M. *Tetrahedron Lett.* **2005**, *46*, 2653.
- (41) Yu, D.; Vladimirov, N.; Frechet, J. M. J. *Macromolecules* **1999**, *32*, 5186.
- (42) Gitsov, I.; Wooley, K. L.; Hawker, C. J.; Ivanova, P. T.; Frechet, J. M. J. *Macromolecules* **1993**, *26*, 5621.
- (43) Gitsov, I.; Hamzik, J.; Ryan, J.; Simonyan, A.; Nakas, J. P.; Omori, S.; Krastanov, A.; Cohen, T.; Tanenbaum, S. W. *Biomacromolecules* **2008**, *9*, 804.
- (44) Gitsov, I.; Fréchet, J. M. J. *Macromolecules* **1993**, *26*, 6536.
- (45) Cho, B. K.; Jain, A.; Gruner, S. M.; Wiesner, U. *Chem. Commun.* **2005**, 2143.
- (46) Chen, C. P.; Dai, S. A.; Chang, H. L.; Su, W. C.; Jeng, R. J. *J. Polym. Sci., Part A: Polym. Chem.* **2005**, *43*, 682.
- (47) Tsai, C. C.; Juang, T. Y.; Dai, S. A.; Wu, T. M.; Su, W. C.; Liu, Y. L.; Jeng, R. J. *J. Mater. Chem.* **2006**, *16*, 2056.
- (48) Dai, S. A.; Juang, T. Y.; Chen, C. P.; Chang, H. Y.; Kuo, W. J.; Su, W. C.; Jeng, R. J. *J. Appl. Polym. Sci.* **2007**, *103*, 3591.
- (49) Ge, Z.; Chen, D.; Zhang, J.; Rao, J.; Yin, J.; Wang, D.; Wan, X.; Shi, W.; Liu, S. *J. Polym. Sci., Part A: Polym. Chem.* **2007**, *45*, 1432.
- (50) Kuo, M. C.; Tung, Y. C.; Yeh, C. L.; Chang, H. Y.; Jeng, R. J.; Dai, S. A. *Macromolecules* **2008**, *41*, 9637.
- (51) Liu, J. K.; Shau, S. M.; Juang, T. Y.; Chang, C. C.; Dai, S. A.; Su, W. C.; Lin, C. H.; Jeng, R. J. *J. Appl. Polym. Sci.* **2011**, *120*, 2411.
- (52) Chang, H. L.; Chao, T. Y.; Yang, C. C.; Dai, S. A.; Jeng, R. J. *Eur. Polym. J.* **2007**, *43*, 3988.
- (53) Juang, T. Y.; Tsai, C. C.; Wu, T. M.; Dai, S. A.; Chen, C. P.; Lin, J. J.; Liu, Y. L.; Jeng, R. J. *Nanotechnology* **2007**, *18*, 205606.
- (54) Tsai, C. C.; Chang, C. C.; Yu, C. S.; Dai, S. A.; Wu, T. M.; Su, W. C.; Chen, C. N.; Chen, F. M. C.; Jeng, R. J. *J. Mater. Chem.* **2009**, *19*, 8484.
- (55) Gitsov, I. *J. Polym. Sci., Part A: Polym. Chem.* **2008**, *46*, 5295.
- (56) Pastoriza-Santos, I.; Liz-Marzán, L. M. *Nano Lett.* **2002**, *2*, 903.
- (57) Davis, R.; Berger, R.; Zentel, R. *Adv. Mater.* **2007**, *19*, 3878.
- (58) Fréchet, J. M. J.; Gitsov, I.; Monteil, T.; Rochat, S.; Sassi, J. F.; Vergelati, C.; Yu, D. *Chem. Mater.* **1999**, *11*, 1267.
- (59) Chang, Y.; Park, C.; Kim, K. T.; Kim, C. *Langmuir* **2005**, *21*, 4334.
- (60) Yang, M.; Wang, W.; Yuan, F.; Zhang, X.; Li, J.; Liang, F.; He, B.; Minch, B.; Wegner, G. *J. Am. Chem. Soc.* **2005**, *127*, 15107.
- (61) Kim, C. K.; Kim, C. K.; Lee, B. S.; Won, J.; Kim, H. S.; Kang, Y. S. *J. Phys. Chem., Part A: Polym. Chem.* **2001**, *105*, 9024.
- (62) Kima, M.; Byun, J. W.; Shin, D. S.; Lee, Y. S. *Mater. Res. Bull.* **2009**, *44*, 334.
- (63) Bouzide, A.; Sauvage, G. *Org. Lett.* **2002**, *4*, 2329.
- (64) Jin, R.; Cao, Y. W.; Mirkin, C. A.; Kelly, K. L.; Schatz, G. C.; Zheng, J. G. *Science* **2001**, *294*, 1901.